Design of Airfoils to Mitigate Wake Bursting

Brent W. Pomeroy* and Michael S. Selig†

University of Illinois at Urbana-Champaign, Department of Aerospace Engineering, Urbana, IL 61801

Strong adverse pressure gradients applied to a wake can cause off-the-surface separation in the wake, which is known as wake bursting. Three high-lift multielement airfoils, consisting of a main element and two flaps, were designed to improve aerodynamic performance and to mitigate wake bursting relative to a baseline airfoil. Two airfoil designs incorporating only modifications to the main-element airfoil are presented for target Reynolds numbers of 1×10^6 and 3×10^6. A third airfoil is presented for which the geometry of the main element and both flaps was modified. The designed airfoils exhibited an increase of C_l/C_d by as much as 17% relative to the baseline geometry as predicted by USM3D, an unstructured RANS solver. Improvements were made by incorporating increased laminar run and improved main-element wake behavior.

Nomenclature

C_d	=	drag coefficient
C_l	=	lift coefficient
C_{m_0}	=	zero-lift pitching moment coefficient
C_p	=	static pressure coefficient
$C_{p,t}$	=	total pressure coefficient
c	=	chord length
D	=	drag
L	=	lift
p	=	static pressure
p_t	=	total pressure
q	=	dynamic pressure
Re	=	Reynolds number
K	=	initial slope of the recovery region
s	=	strength of wake bursting parameter
t/c	=	thickness-to-chord ratio
U_t	=	total velocity
u	=	streamwise velocity component
v	=	transverse (chord-normal) velocity component
x	=	Earth-fixed Cartesian coordinate parallel to the chord line
y	=	Earth-fixed Cartesian coordinate normal to the chord line
α	=	angle of attack
α^*	=	angle of attack for which the velocity distribution is constant
δ	=	absolute flap deflection angle
δ_r	=	relative flap deflection angle
ϕ	=	conformally-mapped airfoil arc limit
τ	=	wake thickness quantified through $C_{p,t}$

Subscripts

∞	=	freestream conditions
le	=	leading edge

*Graduate Research Fellow, Department of Aerospace Engineering, 104 S. Wright St., AIAA Student Member.

†Professor, Department of Aerospace Engineering, 104 S. Wright St., AIAA Associate Fellow.

max = a maximum value
r = relative

Superscripts
$(\tilde{})$ = dimensionless value of variable
$(\bar{})$ = mean value of variable

Acronyms
LTPT = Low-Turbulence Pressure Tunnel
MSES = Multielement Airfoil Design/Analysis System
RANS = Reynolds-Averaged Navier Stokes
TetrUSS = Tetrahedral Unstructured Software System

I. Introduction

High-lift systems are integral to the low-speed performance of transport aircraft, and are also critically important to achieve desired takeoff and landing metrics. Takeoff conditions require the aircraft to takeoff and climb to a given altitude in a minimum amount of time while burning as little fuel as possible. When landing an aircraft, it is desired to decrease the approach and landing speeds by increasing $C_{L,max}$ to minimize landing field length. Aerodynamic performance of a high-lift system can dramatically affect the performance parameters of the entire aircraft, as documented in various trade studies. Preliminary design trade studies for a generic 150-passenger airplane with a range of 2,700 nm suggest a 5% increase in takeoff L/D results in an 11% increase in range for a given payload while a 5% increase in $C_{L,max}$ during landing yields a 20% increase in payload for a given approach speed.[1]

The aerodynamics of multielement high-lift devices is complex and can be greatly impacted by wakes in an adverse pressure gradient. In addition to the shape and location of each element, the wake of the main element, the jet through the gaps, and the flap wakes can all have a large effect on the flowfield. If a strong adverse pressure gradient is imposed on a multielement airfoil, a wake may experience off-the-surface separation, or "wake bursting," while the flow along the surface remains attached. Wake bursting is a local deceleration of the flow in the wake of one or more of the elements. A conceptual sketch of a burst-wake region is presented in Fig. 1. As shown in the drawing, a wake from an element may rapidly thicken and decelerate because of the strong adverse pressure gradient. Both the main element wake and first flap wake are burst in the sketch. Burst wakes are characterized by rapid wake thickening, flow deceleration, and increased turbulence.[2–6] In general, aerodynamic performance of the airfoil is poorer if the wakes of the main element and the flaps become confluent, i.e. if they merge.

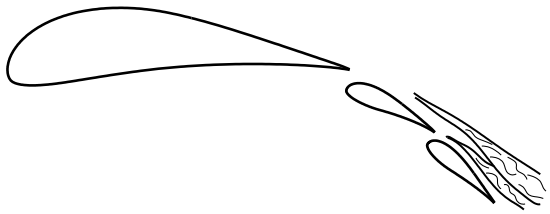

Figure 1. Conceptual sketch of wake bursting over a high-lift multielement airfoil.

Wake bursting, as discussed by Smith,[7] is a viscous phenomenon, leading to an increase in drag (C_d), a reduction of maximum lift $(C_{l,max})$, an effective decambering of the airfoil system, and sometimes flow reversal in the wake.[3–5,8–12] As expected, the pressure distribution of a multielement airfoil can be driven by the wakes in addition to the shape and location of the flap elements.[2,10–14] In fact, if the wakes merge, it has been shown that the momentum deficit in the wakes can dominate the flowfield.[5,12,14–20] Research performed in the NASA Langley Low Turbulence Pressure Tunnel (LTPT) indicated that the development of a wake is highly dependent on the Reynolds number of the flow and that a lower Reynolds number can result in larger wakes and more off-the-surface flow reversal.[13,19] Some previous tests investigated the burst wake of a flat plate with a single flap in an adverse pressure gradient imposed by moveable tunnel walls with no flow curvature.[9,21–23] These flat plate tests concluded that turbulence intensity and wake thickness both increased with a stronger adverse pressure gradient.

Considerable efforts have been made to develop methods which accurately predict high-lift multielement airfoil flowfields, and many of these results have been discussed in great detail during the 1st and 2nd AIAA CFD High-Lift Prediction Workshops.[24–26] Some of the key conclusions of these concentrated efforts indicate that simulations tended to underpredict lift, drag, and the magnitude of pitching moment when compared with experimental data. In general, industry-standard one- and two-equation turbulence models yielded nearly-identical results. Results indicate it may be necessary to accurately model experimental hardware (support brackets and pressure tube bundles) in the simulation when attempting to capture performance near stall. Overall, velocity profiles in the wakes agreed well between most structured and unstructured codes if there was sufficient grid refinement in the wake region.

The objective of this study was to computationally capture burst wakes over a multielement airfoil and to design numerous airfoils to mitigate the presence of wake bursting. A decrease in the strength of wake bursting results in improved aerodynamic performance of the airfoil. Computational tools were utilized to capture wake formation and behavior of the burst wakes for a baseline airfoil. Ultimately, this project aimed to determine the factors which drive the formation of wake bursting and to design a series of airfoils in which the effect of wake bursting upon the flowfield is decreased. Finally, computational simulations were performed to verify the aerodynamic improvement for the newly-designed airfoils.

II. Tools and Methodology

Numerous three-element airfoil systems, consisting of a main element and two flaps, were examined with a variety of tools throughout this research project. Computational simulations were performed using both MSES, a coupled inviscid/viscous solver, and USM3D, an unstructured RANS code. New airfoils were designed using MFOIL, an inverse conformal mapping routine. Each of these tools will now be discussed.

A. Geometry and Coordinate Systems

The baseline airfoil, known as the MFFS(ns)-026 airfoil, is plotted in Fig. 2. This airfoil, consisting of a main element and two flap elements, is similar to the multielement airfoil designed by Ragheb[27] and has been previously studied by the author.[6,12,20] As seen in Fig. 2, the airfoil system is shown at $\alpha = 0$ deg with a system chord length of unity. It is defined that $\alpha = 0$ deg when the leading edge and trailing edge of the main element lie on the x axis as depicted. The airfoil chord length is taken as the distance from the leading edge of the main element to the trailing edge of the last element projected along the main-element chord line. Airfoil coordinates for each element are provided in Ref. 6.

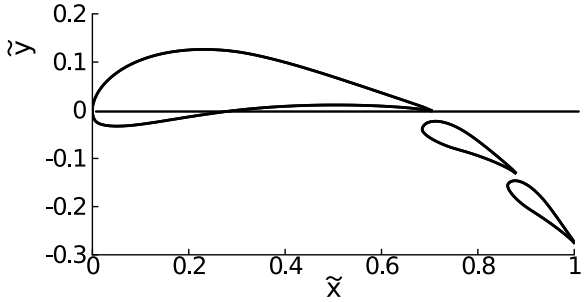

Figure 2. Baseline MFFS(ns)-026 three-element airfoil at $\alpha = 0$ deg.

Two coordinate systems were used to define the location of each element of the airfoil system including a relative and an absolute coordinate system. A relative coordinate system, as shown in Fig. 3(a), could be used to define the system by parameters that govern the flow including gap size, overhang distance, and relative deflection angle. The gap size between elements (gap_n) was defined as the distance from the trailing edge of element n to the closest point on element $n+1$. The overhang distance $(overhang_n)$ between element n and $n+1$ was defined as the distance from the leading edge of element $n+1$ to the trailing edge of n projected along the chord line of element n, as shown in the lower portion of Fig. 3(a). A positive overhang distance indicates the leading edge of element $n+1$ is upstream of the trailing edge of element n, as shown in the figure. Finally, the relative deflection angle (δ_r) for the two flaps was defined relative to the chord line of the previous element. An absolute coordinate system was used to define the location of each element in terms of the leading edge coordinate $(\widetilde{x},\widetilde{y})^{LE}$ and absolute deflection angle δ [see Fig. 3(b)]. Throughout this document, a superscript symbol ($\widetilde{\ }$) indicates a nondimensionalized variable. In this case, $\widetilde{x}$ and $\widetilde{y}$

are nondimensionalized by the system chord length c_{sys} such that

$$\widetilde{x} = \frac{x}{c_{sys}} \tag{1a}$$

$$\widetilde{y} = \frac{y}{c_{sys}}. \tag{1b}$$

As shown in the figure, the downward deflection angle of each flap element was defined relative to the main-element chord line, and a positive deflection angle corresponded to a downward flap deflection.

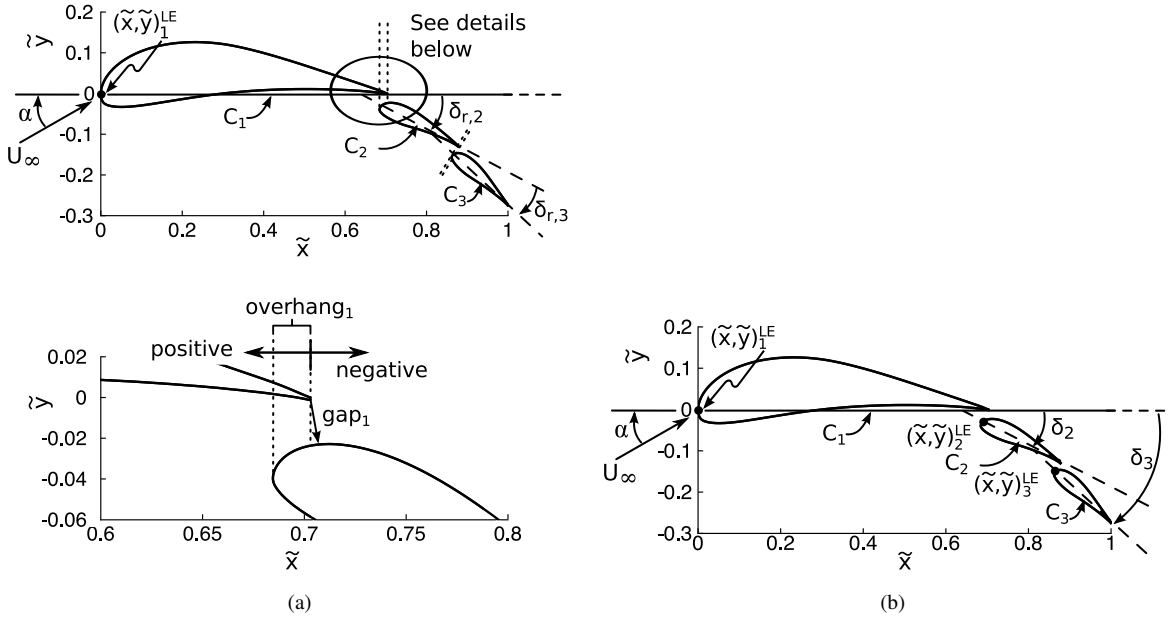

Figure 3. Coordinate systems used to define the three-element airfoil geometry including a) relative coordinates and b) absolute coordinates.

Throughout the course of this project, data were nondimensionalized by characteristic values such that easy comparisons could be made between data sets. In this document, nondimensional values are denoted by either a standard coefficient of the form C_* or by the tilde character ($\widetilde{}$), as previously mentioned. Lift and drag coefficients were defined by the standard equations such that

$$C_l = \frac{l}{q_\infty c} \tag{2a}$$

$$C_d = \frac{d}{q_\infty c} \tag{2b}$$

where q_∞ is the freestream dynamic pressure, c is the airfoil chord length, and l and d are the two-dimensional values of lift and drag, respectively. Per standard definition, the static pressure coefficient was defined by

$$C_p = \frac{p - p_\infty}{q_\infty} \tag{3}$$

in which p denotes the static pressure. A similar coefficient, deemed the total pressure coefficient, was defined by

$$C_{p,t} = \frac{p_t - p_{t,\infty}}{q_\infty} = \frac{\Delta p_t}{q_\infty} \leq 0 \tag{4}$$

for which p_t represents total pressure. A negative value of $C_{p,t}$ indicates a loss in total head while a value of 0 indicates the local total head is equal to the freestream total head. The magnitude of the velocity vector, denoted as the total velocity, is defined by the two components of the velocity vector (u, v) by

$$U_t = \sqrt{u^2 + v^2} \tag{5}$$

and nondimensionalized by the freestream airspeed U_∞

$$\widetilde{U}_t = \frac{U_t}{U_\infty}. \tag{6}$$

B. MSES

The computational tool MSES, developed by the MIT Computational Design Lab, was used to provide a low-order computational prediction of the aerodynamics and flowfield for a given multielement airfoil. MSES v. 3.05, released in July 2007, was utilized throughout these research efforts.[28] MSES is a coupled inviscid/viscid suite of codes that can be used to predict the flow around multielement airfoils and is partially based upon the single-element ISES code, which in turn is partially based upon the single-element XFOIL code as documented in a wide number of papers.[29–37] A two-equation lagged-dissipation integral boundary layer formulation is coupled to an outer streamline-based Euler solution by the displacement thickness, and multi-dimensional Newton iteration is performed to simultaneously solve the viscous and inviscid regions. The steady-state Euler equations are discretized on an intrinsic curvilinear streamline-fixed finite-volume grid, in which the grid and the flowfield are simultaneously solved. Axisymmetric wakes and confluent boundary layers are modeled through a multi-deck integral boundary-layer formulation, and the location and size of wakes shed from multielement airfoils has been found to be somewhat, but not fully, accurate.[20,23,38,39] Transition from laminar to turbulent flow can be specified or predicted. Predictions are based upon the Orr-Sommerfeld equation in which the onset of Tolmein-Schlichting waves provides a manner to predict boundary-layer transition. Coupled inviscid/viscous solvers, such as MSES, are computationally cheaper because results are returned in seconds as compared to a Navier-Stokes solver wherein computations are performed over multiple hours. However, this decrease in cost is associated with a decrease in fidelity. Thus, the potential flow/boundary layer coupled solvers are typically deemed a low-order computational method. As higher-order computational tools were utilized to predict the flowfield, these results are not presented throughout this document. Simulations from MSES were utilized for the sole purpose of determining the laminar-to-turbulent transition point.

C. TetrUSS and USM3D

The Tetrahedral Unstructured Software System (TetrUSS), an unstructured Reynolds-Averaged Navier Stokes (RANS) computational fluid dynamics package developed by NASA Langley, was used in the current research. This suite of loosely-connected programs consists of geometry preparation tools, a grid generator, a computational solver, and postprocessing routines. An assortment of parallelization utilities are also provided with the package.[40–47] Three-dimensional unstructured grids, generated using the advancing-front and advancing-layers techniques, were created using VGrid 4.1. A version of USM3D 6.0, including a the NEWTL laminar-to-turbulent transition module, was used throughout this research project. This NEWTL module, which can only be used with the one-equation Spalart-Almaras turbulence model, declares laminar flow for a user-specified range of upper- and lower-surface coordinates and turbulent flow over the remainder of the surface.

D. MFOIL/PROFOIL

An inviscid multipoint inverse design airfoil method was utilized to design the multielement airfoils in this project. While the direct-design method, in which the designer specifies the shape of the airfoil and the aerodynamic performance is determined from the shape, can be used, the more-desirable inverse design approach was implemented in this research. Contrary to the direct-design routines depicted in Fig. 4(a), inverse-design techniques yield an airfoil shape based upon various aerodynamic performance values and/or geometric constraints. In this way, the aerodynamic performance of an airfoil is easily controlled, and the airfoil shape that yields the desired performance is the output. One such inverse design method is to specify portions of the inviscid C_p distribution, or velocity distribution, and subsequently determine the appropriate airfoil shape, as shown in Fig. 4(b). The MFOIL user interface, coupled to PROFOIL, was used to control and develop the desired pressure distributions over the airfoil.[48–56] This software allows the user to specify different design angle of attack values relative to a zero-lift line at different locations on the airfoil. As the airfoil is discretized into a number of segments, the user is able to have a great deal of control over the resulting airfoil performance, especially by controlling the inviscid velocity distribution over a given airfoil segment. It is possible to specify the design angle of attack, α^*, for a segment either directly or by determining the value through a multidimensional Newton iteration process in which additional constraints, either geometric or otherwise, are satisfied. All airfoils designed during the course of this project were specified with constant velocity distributions along a given segment. The arc limits for the segment at which α^* is specified are bounded by two values of ϕ which

correspond to the arc limits for the conformal-mapped circle. In this project, the ϕ limits were selected to be 0 and 60 deg. Each airfoil element is designed in isolation, and the multielement airfoil is assembled with the three isolated airfoil designs.

Numerous improvements and enhancements were made to the MFOIL design code that increased functionality for multielement airfoil design. Methods were implemented such that the user could specify the location of an element in relative coordinates in addition to absolute coordinates.[20] In addition, MSES was integrated into the MFOIL suite of programs to yield rapid viscous analysis capability to the user. It is noted that the design routines still rely upon the inviscid conformal-mapping techniques, and that MSES is utilized solely for analysis purposes.

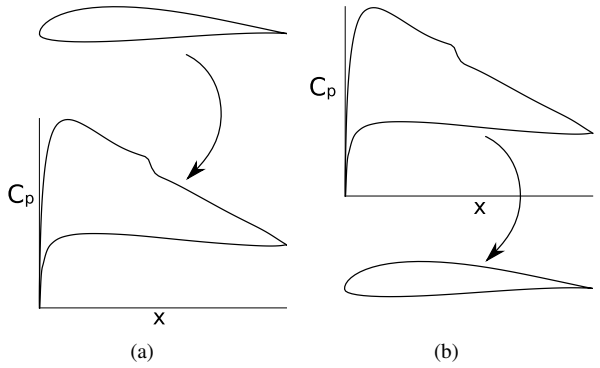

Figure 4. Conceptual representation of a) direct-design and b) inverse-design methods.

III. Baseline Airfoil

A. Airfoil Geometry

The three-element MFFS(ns)-026 airfoil, shown in Fig. 2 consisting of a main element and two flaps, serves as the baseline airfoil against which the designed airfoils are compared.[6,12,20,27] While the elemental airfoil coordinates and relative chord lengths for the baseline airfoil remain unchanged from the geometry presented in Ref. 6, the flaps are rigged in a slightly different location for the baseline airfoil. Table 1 presents the flap riggings for the baseline airfoil in relative coordinates including gap size, overhang distance, and relative deflection angle as defined in Sec. II A. Absolute coordinates, including leading edge point and absolute deflection angle, as well as the relative chord lengths for the airfoil are shown in Table 2.

Table 1. Baseline Airfoil Flap Rigging in Relative Coordinates

Main Element to Flap 1	gap_1	0.026
	$overhang_1$	0.015
	$\delta_{r,1}$	26.3 deg
Flap 1 to Flap 2	gap_2	0.015
	$overhang_2$	0.002
	$\delta_{r,2}$	16.3 deg

Table 2. Baseline Airfoil Flap Rigging in Absolute Coordinates

Main Element	$(\widetilde{x},\ \widetilde{y})_1^{LE}$	(0, 0)
	δ_1	—
	c_1	0.700
Flap 1	$(\widetilde{x},\ \widetilde{y})_2^{LE}$	(0.686, −0.037)
	δ_2	26.4 deg
	c_2	0.213
Flap 2	$(\widetilde{x},\ \widetilde{y})_3^{LE}$	(0.865, −0.151)
	δ_3	42.6 deg
	c_3	0.182

The aforementioned MFOIL/PROFOIL suite of codes can be used to design a multielement airfoil utilizing inverse methods through conformal mapping techniques and multidimensional Newton iterations. The MFFS(ns)-026 airfoil was designed by Ragheb[27] through the specification of upper- and lower-surface α^*-ϕ curves as well as numerous inverse-design parameters. Figure 5 shows the α^*-ϕ curves for the upper and lower surfaces of all three airfoil elements. As seen in the figure, small circles represent the ϕ values bounding each segment such that the relationship

between the α^*-ϕ curve and resulting airfoil geometry can be readily observed. The laminar-to-turbulent transition behavior significantly affects the performance of low-Reynolds-number airfoils, and this transition behavior is controlled with the α^*-ϕ curve. As seen in Fig. 5(g), the resulting airfoil geometry is coplotted with the control points. More control points are specified on the upper surfaces than the lower surfaces as more control of the upper surface was desired than the lower surface. All α^*-ϕ curves are defined by linear or piecewise-linear functions. While the α^*-ϕ curve can be used to control the upstream portion of the pressure-recovery region, the *REC* parameter controls the downstream portion of the adverse-pressure gradient. It is noted that the K parameter affects the initial slope of the pressure-recovery pressure distribution, K_s is used to control the airfoil thickness and resulting pressure distribution near the trailing edge, C_{m_0} defines the zero-lift pitching moment, and $(t/c)_{max}$ specifies the maximum thickness-to-chord ratio based upon the elemental chord length.

Table 3. Inverse-Design Parameters for MFFS(ns)-026 Airfoil

	Main Element	Flap 1	Flap 2
K_u	0.05	0.20	0.20
K_l	0.20	0.20	0.20
K_s	0.30	0.15	0.15
C_{m_0}	-0.20	-0.16	-0.10
$(t/c)_{max}$	0.200	0.205	0.205

B. Performance at $Re = 1 \times 10^6$

The MFFS(ns)-026, introduced earlier in Sec. III A, was computationally analyzed using two different codes executed in C_l-matching mode for a specified C_l of 3.40, corresponding to $\alpha = -0.100$ deg at Re of 1×10^6. MSES, a lower-fidelity viscous/inviscid coupled solver, was used to predict the transition points for the airfoil. These transition points were then used to execute higher-fidelity fixed-transition simulations in USM3D. While results from both of these solvers are presented in this section, the majority of the discussion is related to the USM3D analyses.

1. *Transition Points*

The resulting viscous C_p distribution predicted by MSES is shown in Fig. 6 in which the pressure distribution is coplotted with the MFOIL control points. The main-element upper surface exhibits a wide pressure peak thus resulting in a more-forgiving geometry for a wider range of α than if a sharp, narrow pressure peak were observed. A strong adverse pressure gradient is observed over the main-element upper surface which, in part, results in larger values of C_l for the airfoil. Increased dumping of C_p for multielement airfoils relative to a single-element airfoil results in C_p being dumped at -1.09 and -0.264 for the main element and flap 1, respectively. Numerous sharp increases in C_p, indicative of laminar-to-turbulent flow transition, are observed over the upper surface of each element. As the flowfield is significantly affected by the main-element aerodynamic performance, the importance of the main-element transition behavior cannot be understated. Increased $\widetilde{x}$ for which laminar flow exists, also known as an increased laminar run, yields a smaller boundary layer at the trailing edge of the main element when compared to a decreased laminar run for a given pressure gradient. However, classic boundary-layer theory indicates that a boundary layer in a strong adverse pressure gradient is larger and thicker than a boundary layer in a weaker, or non-existent, pressure gradient. Thus, the boundary-layer thickness over the airfoil can be controlled by both the transition point and the magnitude of the pressure-recovery gradient. The values for each of the transition locations are presented in Table 4. Fully-laminar flow was predicted over the lower surface of all three airfoils, and no transition was observed. This fact is reflected in the table.

2. *Aerodynamic Performance and Resulting Flowfield*

USM3D, the previously-discussed unstructured RANS solver, was used to computationally predict the aerodynamics of the MFFS(ns)-026 airfoil at $C_l = 3.40$ and $Re = 1 \times 10^6$. Transition points predicted by MSES, shown in Table 4, were declared through the NEWTL laminar-to-turbulent transition package to the USM3D flow solver. The resulting flowfield, including total velocity ($\widetilde{U}_t$, defined in Eq. 6) and the nondimensional head-loss coefficient ($C_{p,t}$, defined

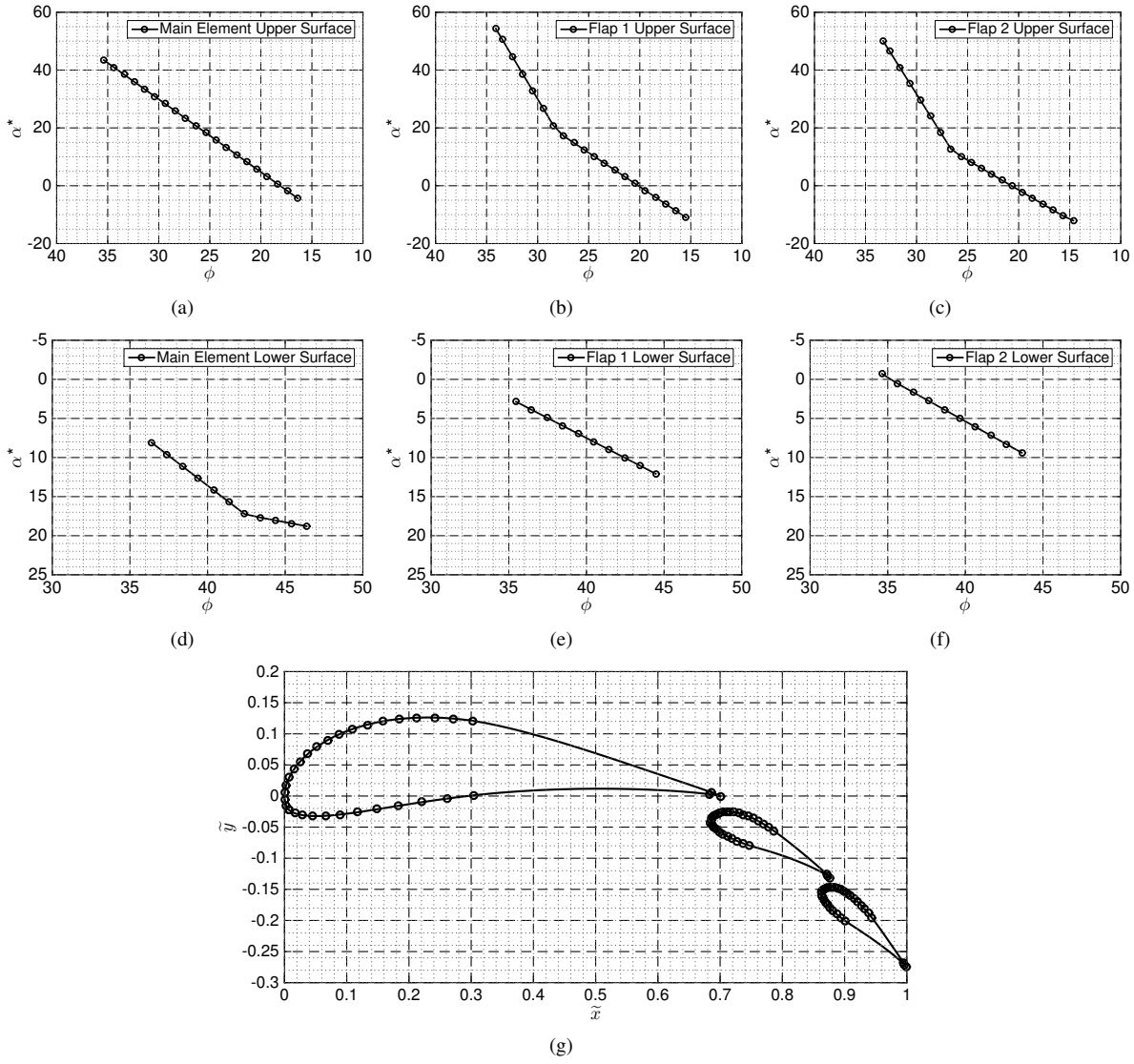

Figure 5. Specified α^*-ϕ distribution for MFFS(ns)-026 including (a) main-element upper surface, (b) flap 1 upper surface, (c) flap 2 upper surface, (d) main-element lower surface, (e) flap 1 lower surface, (f) flap 2 lower surface, and (g) resulting geometry coplotted with control points.

Table 4. Transition Points ($\widetilde{x}$) for MFFS(ns)-026 at $C_l = 3.40$ and $Re = 1 \times 10^6$

Main Element	Upper Surface	0.263
	Lower Surface	0.700 (trailing edge)
Flap 1	Upper Surface	0.783
	Lower Surface	0.876 (trailing edge)
Flap 2	Upper Surface	0.937
	Lower Surface	1.000 (trailing edge)

in Eq. 4), is shown in Fig. 7. Both a wide and zoomed-in view are shown, wherein the zoomed-in view presents the downstream portion of flap 1, the entirety of flap 2, and the wake region downstream of the airfoil trailing edge. Data presented in the zoomed-out view are coplotted with the computational mesh to facilitate easy comparison between the mesh and the computed flowfield. As seen in the figure, wakes are observed to trail behind the main element, flap 1, and flap 2, as evidenced by decreases in both $\widetilde{U}_t$ and $C_{p,t}$. Boundary layers over both the upper and lower surface are

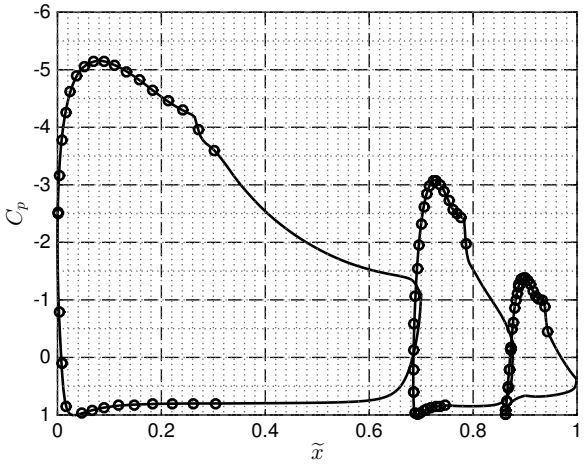

Figure 6. Viscous C_p distribution for baseline MFFS(ns)-026 at $\alpha = 0.00$ deg and $Re = 1 \times 10^6$ as predicted by MSES coplotted with MFOIL control points.

shed as a wake at the trailing edge of each element. The main-element wake, the largest of all three wakes, shows a large momentum-deficit region downstream of the airfoil trailing edge ($\widetilde{x} \geq 1.02$), and the size of this wake, or the size of the momentum-deficit region, increases with further distance downstream of the airfoil trailing edge. While the main-element wake continually thickens with increasing downstream distance, the largest growth rate for this wake occurs for which $0.95 < \widetilde{x} < 1.01$. Despite the rapid growth of the main-element wake, no merging is observed between the main-element and flap 1 wake. However, the flap 1 and flap 2 wakes merge and interact immediately downstream at $\widetilde{x} = 1.05$. The small, thin boundary layers shed from flap 1 results in a narrow, thin wake that exhibits significant wake thickening in the pressure recovery region, or $0.90 < \widetilde{x} < 1.00$. Careful investigation of the flow over flap 2 shows a somewhat large boundary layer over the upper surface. Streamlines in the flowfield surrounding flap 2, plotted in Fig. 7(f), indicate a small recirculation region over the upper surface flap 2 for $0.92 < \widetilde{x} < 0.95$. This separation region results in markedly increased boundary-layer thickness at the trailing edge of flap 2, thus yielding a thicker wake than if a recirculation region were not present.

Aerodynamic performance metrics for the MFFS(ns)-026 airfoil at C_l of 3.40 and Re of 1×10^6 were calculated in which significant lift is evidenced by the highly-curved flowfield plotted in Fig. 7(e). Despite the large value of C_l, the existence of the large momentum-deficit region results in C_d of 0.0470, an elevated value relative to a condition for which wake bursting is not observed. In addition to increased C_d, the burst wake effectively decambers the airfoil system, or reduces the overall streamline curvature, thus corresponding to decreased lift for the system than for a non-burst flowfield. Overall, the aerodynamic efficiency of this airfoil is computed to be 72.3. A well-designed multielement airfoil would yield large C_l without elevated C_d, thus resulting in increased C_l/C_d relative to the baseline airfoil.

Figure 8 presents wake profiles at a range of $\widetilde{x}$ values from the flowfield previously plotted in Fig. 7. These wake cuts are shown close to the airfoil trailing edge for $\widetilde{x} = (1.025, 1.050, 1.075, 1.100)$ in Fig. 8(a) and across a wider wake range of $\widetilde{x} = (1.100, 1.200, 1.300, 1.400)$ in Fig. 8(b). Consider, first, the development of the wakes immediately downstream of the airfoil trailing edge, seen in Fig. 8(a), shows the large main-element wake and the merging between the two flap wakes. Throughout this paper, the minimum value of $\widetilde{U}_t$ at a given value of $\widetilde{x}$ will be presented as $\widetilde{U}_{t_{min}}|_{\widetilde{x}}$ in which the subscript $\widetilde{x}$ indicates the streamwise coordinate at which the wake profile is taken. While $\widetilde{U}_{t_{min}}|_{\widetilde{x}=1.025}$ is observed in the flap 2 wake, this point occurs in the main-element wake at all other values of $\widetilde{x}$. As also seen above in Fig. 7, $\widetilde{U}_{t_{min}}|_{\widetilde{x}}$ decreases with downstream distance over the range $1.025 \leq \widetilde{x} \leq 1.10$. Throughout this region, a marked decrease in $\widetilde{U}_{t_{min}}$ from 0.652 to 0.518 results in a 25.9% decrease in the minimum velocity. A rapid increase in wake thickness over a small spatial range, such as that observed for $1.025 < \widetilde{x} < 1.075$, is a typical characteristic of a burst wake. The wakes are observed to move in a $-\widetilde{y}$ direction for increased $\widetilde{x}$, as expected due streamline curvature. As previously stated, the main-element wake is the thickest of all three wakes for the entire range of $\widetilde{x}$ downstream of the trailing edge. While the two flaps yield two separate wakes at $\widetilde{x} < 1.050$, the aforementioned merging between the two flap wakes is further evidenced in the wake profiles. Increased downstream distance corresponds to an increase in the confluence between the two flap wakes. Figure 8(b) shows wake profiles at a wider range of $\widetilde{x}$ from 1.100 to 1.400. A large decrease in $\widetilde{U}_{t_{min}}|_{\widetilde{x}}$ is observed for $\widetilde{x} < 1.100$, as previously observed, but smaller decreases in $\widetilde{U}_{t_{min}}$ are observed

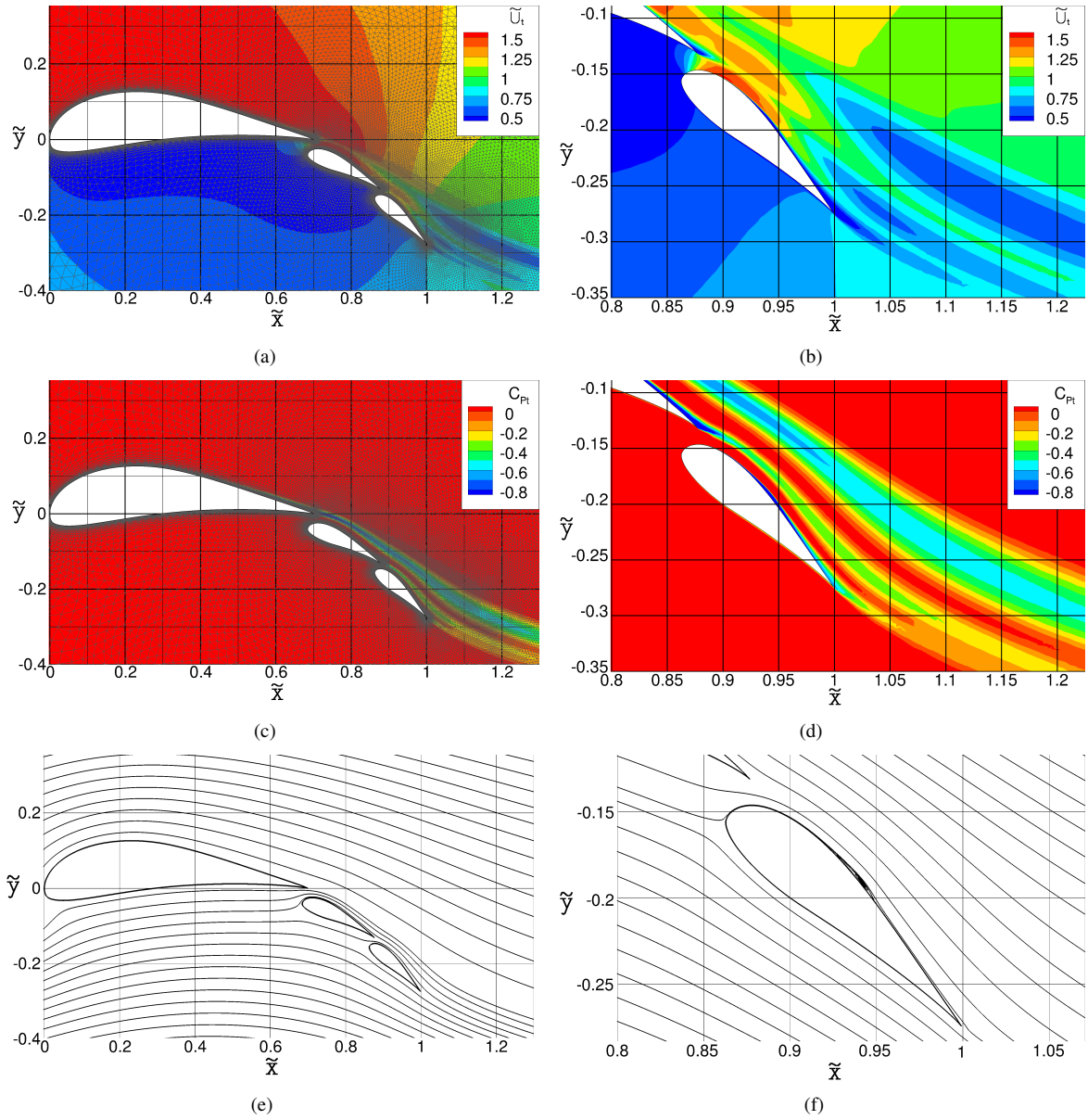

Figure 7. Flowfield for MFFS(ns)-026 at $C_l = 3.40$ and $Re = 1 \times 10^6$ evidenced by (a) wide view of $\widetilde{U}_t$, (b) zoomed view of $\widetilde{U}_t$, (c) wide view of $C_{p,t}$, (d) zoomed view of $C_{p,t}$, (e) wide view of streamlines, and (f) detailed view of streamlines surrounding flap 2 indicating small separation on the upper surface.

downstream of $\widetilde{x} = 1.100$. These trends indicate that a global minimum of $\widetilde{U}_t$ exists near $\widetilde{x} \approx 1.1$. This point was, in fact, calculated to be $\widetilde{x} = 1.133$ at which $\widetilde{U}_{t_{min}}|_{\widetilde{x}} = 0.509$. Increased wake interaction between the two flap wakes is observed for increasing downstream distance until the two wakes are fully merged at $\widetilde{x} \approx 1.2$. Both the main-element wake and the flap wake are observed to thicken and exhibit monotonically-increasing $\widetilde{U}_{t_{min}}|_{\widetilde{x}}$.

C. Performance at $Re = 3 \times 10^6$

In addition to the previously-presented results, the MFFS(ns)-026 airfoil presented in Sec. III A was analyzed at a freestream Reynolds number of 3×10^6 for $C_l = 3.40$, corresponding to $\alpha = -0.682$ deg. Computational data, similar to that presented in the previous subsection, as predicted by both MSES and USM3D, are shown herein.

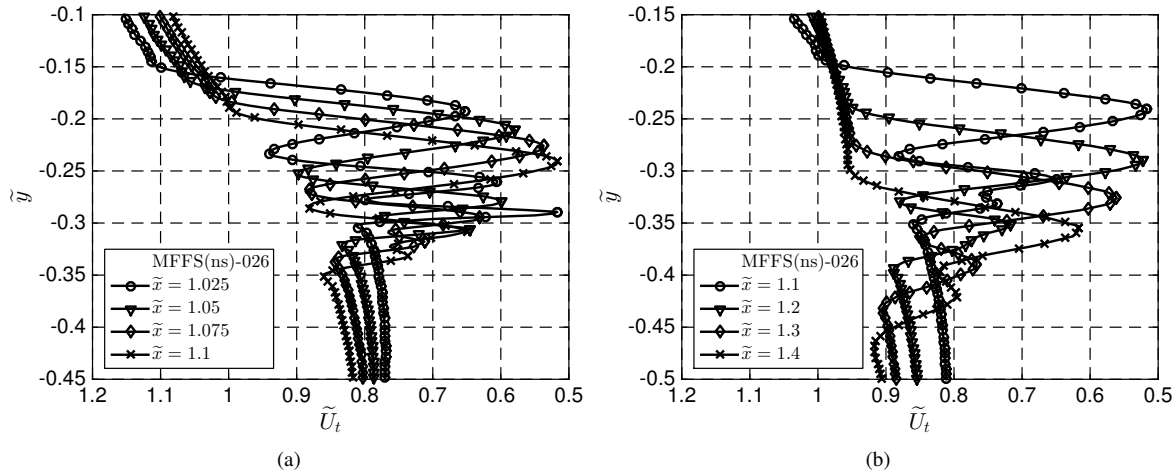

Figure 8. Wake profiles for MFFS(ns)-026 at $C_l = 3.40$ and $Re = 1 \times 10^6$ for (a) $1.025 \leq \widetilde{x} \leq 1.100$ and (b) $1.100 \leq \widetilde{x} \leq 1.400$.

1. Transition Points

MSES was used to simulate the MFFS(ns)-026 airfoil to determine the transition points over all three airfoil elements. As discussed in Sec. III A, the importance of the relationship between the α^*-ϕ curves, pressure distribution, and transition points cannot be understated. Therefore, the MSES-predicted C_p curve is shown in Fig. 9 coplotted with the ϕ points around each airfoil element. Similar to the results at $Re = 1 \times 10^6$ shown in Fig. 6, the pressure peak over the main-element is elevated over a wide range of $\widetilde{x}$ after which the pressure is aggressively recovered to C_p of -1.07 at the main-element trailing edge. Static pressure is recovered over flap 1 and dumped from the trailing edge into the outer flow at $C_p = -0.250$. Sharp increases in C_p, associated with transition from laminar to turbulent flow, are observed over the upper surface of all three elements. These points, presented in Table 5, occur at an upstream location relative to the aforementioned data at $Re = 1 \times 10^6$. As was the case for the simulation at $Re = 1 \times 10^6$, no transition was observed over the lower surface of any airfoil elements.

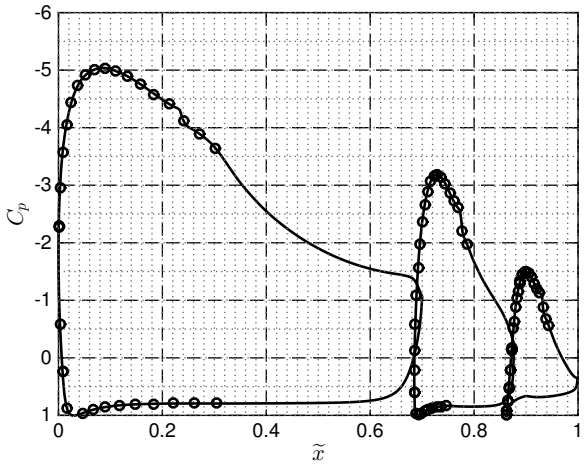

Figure 9. Viscous C_p distribution for MFFS(ns)-026 at $C_l = 3.40$ and $Re = 3 \times 10^6$ as predicted by MSES coplotted with MFOIL control points.

2. Aerodynamic Performance and Resulting Flowfield

Fixed-transition RANS computations were performed at $C_l = 3.40$ deg and $Re = 3 \times 10^6$, and results are plotted in Fig. 10. The main-element wake is burst, and a large momentum-deficit region is seen near the trailing edge of the airfoil. This wake monotonically thickens with increasing downstream distance immediately downstream of the

Table 5. Transition Points ($\widetilde{x}$) for MFFS(ns)-026 at $C_l = 3.40$ and $Re = 3 \times 10^6$

Main Element	Upper Surface	0.233
	Lower Surface	0.700 (trailing edge)
Flap 1	Upper Surface	0.774
	Lower Surface	0.877 (trailing edge)
Flap 2	Upper Surface	0.931
	Lower Surface	1.000 (trailing edge)

airfoil trailing edge. Rapid wake thickening is observed in the main-element wake for the range $0.960 < \widetilde{x} < 1.03$. These results indicate that the wakes burst slightly further downstream than the wakes for $Re = 1 \times 10^6$, which were observed to rapidly grow for $\widetilde{x} < 0.950 < \widetilde{x} < 1.01$. It is also noted that the rapid wake growth for $Re = 3 \times 10^6$ occurs over a narrower range of $\widetilde{x}$ than for the lower-Reynolds-number case. In addition, the three wakes at the higher Reynolds number exhibit decreased momentum deficit when compared to the simulation at $Re = 1 \times 10^6$ in Fig. 7, which is the expected trend as viscous wakes and boundary layers thin with increasing Reynolds number. Results show that the wakes from flap 1 and flap 2 do not merge for $\widetilde{x} < 1.2$. The reader is reminded that the $Re = 1 \times 10^6$ flowfield contained merging flap wakes at $\widetilde{x}$ as low as 1.100. No surface separation is observed over the flap 2 upper surface for the higher-Reynolds-number case. Aerodynamic performance metrics were determined for a $C_l = 3.40$ and $\alpha = -0.781$, $C_d = 0.0407$, and $C_l/C_d = 83.5$. Decreased α for the desired C_l, decreased C_d, and the resulting increased C_l/C_d are observed at Re of 3×10^6 when compared with the analysis at 1×10^6. In particular, C_l/C_d for the case at which $Re = 3 \times 10^6$ is calculated to be 83.5, which is 15.5% larger than the value of 72.3 at 1×10^6. It is noted that the α for which $C_l = 3.40$ is -0.781 and -0.682 for the USM3D and MSES results, respectively.

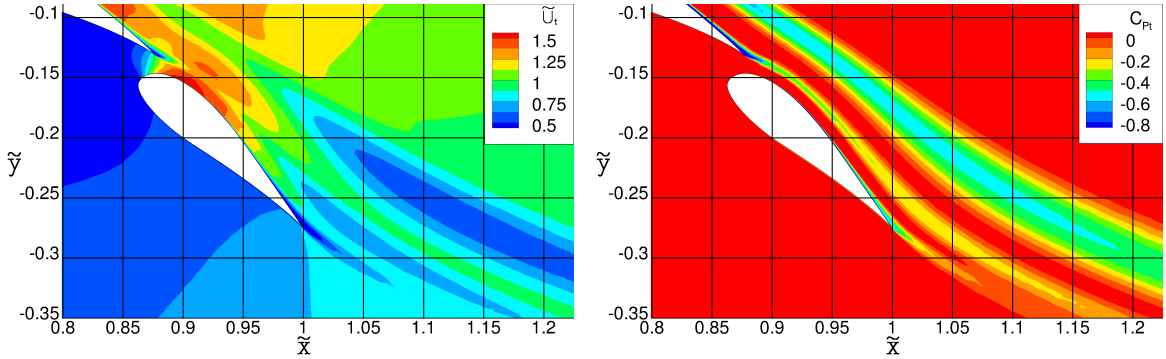

(a) (b)

Figure 10. Flowfield for MFFS(ns)-026 at $C_l = 3.40$ and $Re = 3 \times 10^6$ evidenced by zoomed views of (a) $\widetilde{U}_t$ and (b) $C_{p,t}$.

A series of wake slices, taken from Fig. 10, for a range of $\widetilde{x}$ between 1.05 and 1.30 are shown in Fig. 11. Figure 10(a) present results for $1.025 \leq \widetilde{x} \leq 1.100$, or the region immediately downstream of the trailing edge while data over a wider range of $\widetilde{x}$, between 1.05 and 1.30, are shown in Fig. 10(b). Consider the four wake profiles taken immediately downstream of the trailing edge as presented in Fig. 10(a). Three separate wakes, including a main-element wake and a wake from each flap, are visible for $1.025 < \widetilde{x} < 1.100$, the full range of $\widetilde{x}$ seen in the figure. The large and thick main-element wake dominates the flowfield for all $\widetilde{x}$. In addition to elevated thickness, the main-element wake contains $\widetilde{U}_{t_{min}}|_{\widetilde{x}}$ at all $\widetilde{x} > 1.025$. While $\widetilde{U}_{t_{min}}|_{\widetilde{x}}$ decreases with increasing $\widetilde{x}$ downstream of 1.025, the largest decreases in $\widetilde{U}_{t_{min}}|_{\widetilde{x}}$ occur at upstream locations rather than at downstream locations. Some interactions are observed between the flap wakes, but these wakes do not merge into one fully-confluent wake for $\widetilde{x} \leq 1.200$. Overall, striking similarities in trends are observed between Figs. 11 and 8. Additional wake slices for $1.100 \leq \widetilde{x} \leq 1.300$ are shown in Fig. 11(b). A slight increase in $\widetilde{U}_{t_{min}}|_{\widetilde{x}}$ is observed between $\widetilde{x}$ of 1.100 and 1.200, and larger increases are observed for $\widetilde{x} > 1.200$. The wake profiles suggest fully-merged flap wakes for $\widetilde{x} > 1.200$.

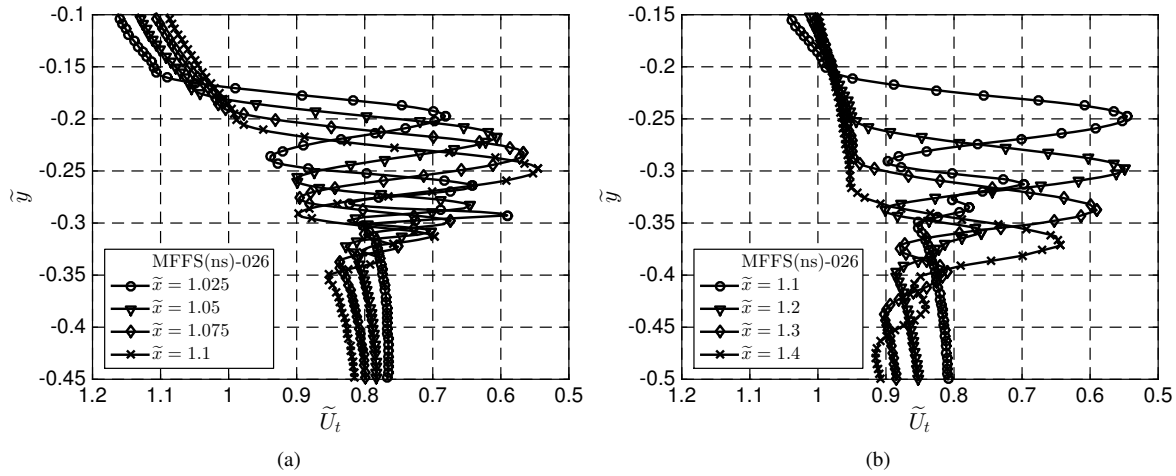

Figure 11. Wake profiles for MFFS(ns)-026 at $C_l = 3.40$ and $Re = 3 \times 10^6$ for (a) $1.025 \leq \widetilde{x} \leq 1.100$ and (b) $1.100 \leq \widetilde{x} \leq 1.400$.

D. Metrics to Quantify Wake Bursting

While the previously-presented computational results are discussed in great detail, no metrics exist in which the results of two different burst-wake flowfields can be readily compared. Consequently, two novel metrics were developed to quantify these flowfields. A threshold was developed to quantify the spatial point at which the wake is said to be burst, and a second threshold was formulated to quantify the extent to which a wake is burst.

1. Spatial Point of Wake Bursting

If a computational or experimental data set indicates the existence of a burst wake, it is possible to determine the spatial point at which the wake begins to burst. Consider, again, Fig. 7 in which contour plots of $\widetilde{U}_t$ and $C_{p,t}$ are presented for the MFFS(ns)-026 at $\alpha = 0$ deg and $Re = 1 \times 10^6$. Qualitatively, the wake thickness is observed to monotonically increase with increasing $\widetilde{x}$ with moderate wake thickening immediately downstream of the main-element trailing edge and rapid wake thickening above and downstream of flap 2. It is desired to quantitatively define the spatial point $\widetilde{x}$ at which the wake not only thickens, but can be said to be burst. A single-line contour plot for $C_{p,t} = -0.5$, extracted from Fig. 7(c,d), is plotted in Fig. 12. In the figure, a large region bounded by $C_{p,t} = -0.5$ exists behind the main-element airfoil, and a small region is seen to exist immediately downstream of flap 1. The main-element wake is the only wake of interest throughout the remainder of this section, and thus the flap 1 and flap 2 wakes will not be addressed. As seen in the figure, the variable τ is defined to be the distance between the upper and lower edges at a given $\widetilde{x}$.

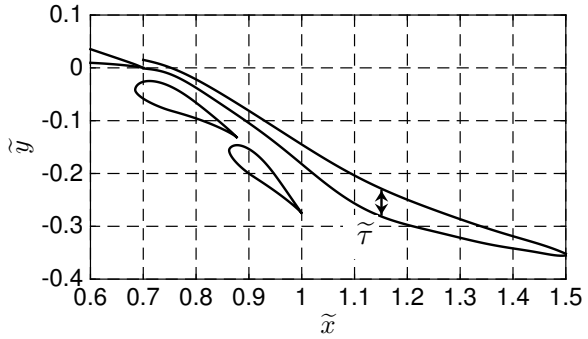

Figure 12. Contour line of of $C_{p,t} = -0.5$ showing definitions of wake thickness τ.

Simulations were performed on the MFFS(ns)-026 at $Re = 1 \times 10^6$ for α between -8 and 8 deg, and Fig. 13 shows results for α of -2, 0, and 2 deg. Figure 13(a) presents τ as a function of downstream distance in which a solid, dashed, and dashed-dotted line correspond to cases for α of -2, 0, and 2 deg, respectively. For all three cases, the

wake depth is observed to increase with respect to $\widetilde{x}$, and increasing α also results in increased τ, as expected. For an α increase of 2 deg, τ_{max} increases by approximately 50% relative to the lower-α condition. Rapid increases in τ are observed across a wide range of τ for α of -2 and 0 deg, but little change in τ is observed for the $\alpha = -2$ case downstream of $\widetilde{x} \approx 0.88$. It is also noted that $\widetilde{x}$ for τ_{max} moves downstream with increasing α.

The rate of increase in τ, $\partial\tau/\partial\widetilde{x}$, is plotted in Fig 13 for the same three α in which increased growth rate is observed for higher-α cases than for lower-α cases. A small $\partial\tau/\partial\widetilde{x}$ gradient for $\alpha = -2$ deg is observed for $\widetilde{x} > 0.88$, corresponding to the aforementioned slow growth in τ. At α of 0 and 2 deg, however, rapid increases in τ result from elevated $\partial\tau/\partial\widetilde{x}$ for a wide range of $\widetilde{x}$. It is this increase in $\partial\tau/\partial\widetilde{x}$ that yields the elevated τ for the higher-α cases in Fig. 13(a).

The curvature of the τ-$\widetilde{x}$ curve, or $\partial^2\tau/\partial\widetilde{x}^2$, is plotted in Fig. 13(c) for the same three conditions. Similar to both τ and $\partial\tau/\partial\widetilde{x}$, the three curves present similar trends with differing magnitudes. As seen in the figure, the $\widetilde{x}$ point for whit $(\partial^2\tau/\partial\widetilde{x}^2)_{max}$ occurs, referred to as $\widetilde{x}_b$, occurs at similar $\widetilde{x}$ for all three conditions. The peak of each $\partial^2\tau/\partial\widetilde{x}^2$ curve is plotted with a single symbol, thus indicating the value of $\widetilde{x}_b$, or the "burst point." As evidenced by Fig. 13(c), the value of $\widetilde{x}_b$ remains largely unchanged for the three different conditions. Figure14 shows the relationship between $\widetilde{x}_b$ for a wide range of α at $Re = 1 \times 10^6$. As seen in Fig 14, and further evidenced in Fig. 13(c), the effect of α upon $\widetilde{x}_b$ is small, but a general trend of increasing $\widetilde{x}_b$ with increasing α is observed.

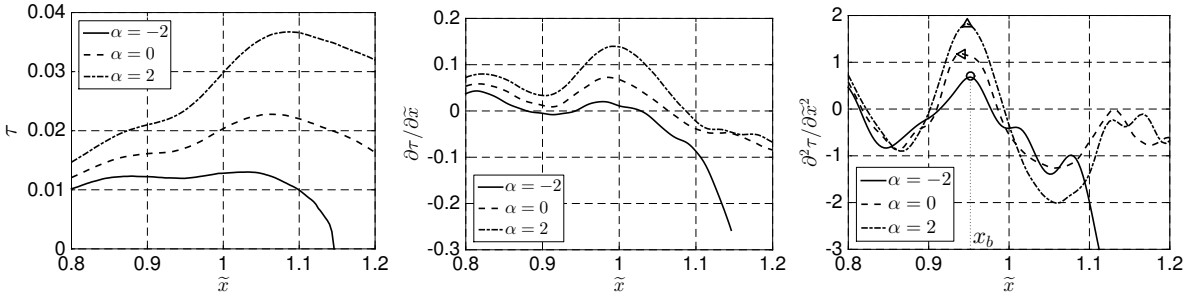

Figure 13. Effect of α for MFFS(ns)-026 at $Re = 1 \times 10^6$ evidenced by (a) τ, (b) $\partial\tau/\partial\widetilde{x}$, and (c) $\partial^2\tau/\partial\widetilde{x}^2$.

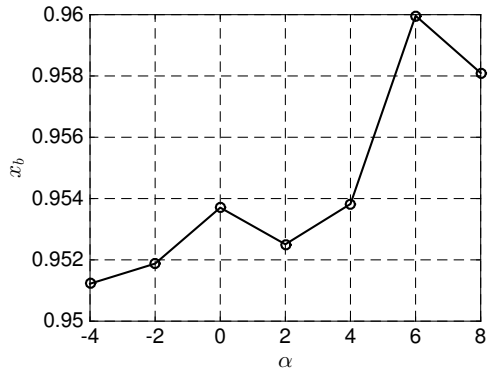

Figure 14. Point of wake bursting $\widetilde{x}_b$ for MFFS(ns)-026 at $Re = 1 \times 10^6$ and range of α.

2. *Strength of Wake Bursting*

In addition to quantifying the burst point, it is also desired to present a global metric to quantify the extent to which a wake is burst, deemed as the strength of wake bursting. As seen in Fig. 12, a contour line of $C_{p,t} = -0.5$ encloses a large momentum-deficit region for the main-element wake. Similar to the previously-discussed $\widetilde{x}_b$, the flap-1 wake is not of interest with regards to this metric. In the figure, a portion of the main-element wake is enclosed by the constant-contour line, denoted as $\widetilde{s}$, which can be calculated by

$$\widetilde{s} = \int_{\widetilde{x}_{min}}^{\widetilde{x}_{max}} (\widetilde{y}_u - \widetilde{y}_l) d\widetilde{x} \tag{7}$$

in which $\widetilde{y}_u$ and $\widetilde{y}_l$ are the upper and lower bounds for the contour line for a given $\widetilde{x}$. The limits of the integral, $\widetilde{x}_{min}$ and $\widetilde{x}_{max}$, correspond to the upstream and downstream limits for which $C_{p,t} = -0.5$. Conceptually, increased $\widetilde{s}$ results from thick wakes in a wide range of $\widetilde{x}$, while decreased $\widetilde{s}$ corresponds to smaller, thinner wakes. Simulations at a variety of α indicate a direct relationship between $\widetilde{s}$ and α, as seen in Fig. 15. In an effort to quantify the extent of wake bursting, threshold values of $\widetilde{s}$ are proposed to define a wake as not burst, moderately burst, or severely burst. As shown in the figure, a wake is defined to be slightly burst for which $\widetilde{s} \leq 0.010$, moderately burst for $0.010 < \widetilde{s} < 0.030$, and severely burst if $\widetilde{s} \geq 0.030$. These threshold values were selected after meticulous examination of computational results across a wide range of α.

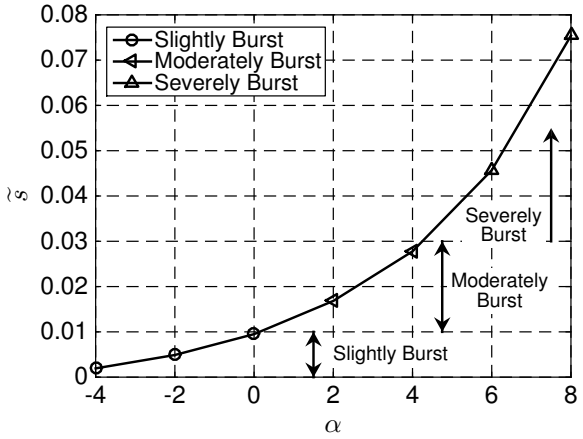

Figure 15. Strength of wake bursting $\widetilde{s}$ as a function of α for $Re = 1 \times 10^6$.

These same metrics, $\widetilde{x}_b$ and $\widetilde{s}$, were calculated for the MFFS(ns)-026 airfoil at $\alpha = 0$ deg and $Re = 3 \times 10^6$. As evidenced by Fig. 10, decreased bursting is observed for the higher-Reynolds number results than for Re of 1×10^6. While numerous differences between the two flowfields are noticed, the burst point of the higher-Reynolds-number flow, calculated to be $\widetilde{x}_b = 0.952$, is only slightly upstream of the flow at Re of 1×10^6 for which $\widetilde{x}_b = 0.954$. Figure 10, presenting results at Re of 3×10^6 depicts a smaller momentum-deficit region than for Re of 1×10^6 shown in Fig. 7. This momentum-deficit region yields $\widetilde{s} = 0.0056$, which is less than $\widetilde{s} = 0.0095$ for $Re = 1 \times 10^6$.

IV. Main-Element Modifications at $Re = 1 \times 10^6$

As the poor aerodynamic performance of the MFFS(ns)-026 airfoil shown in Fig. 7 is partially attributed to the burst wakes, it was desired to design an airfoil with superior aerodynamic performance and wake development relative to the MFFS(ns)-026 airfoil at the same design point for which $Re = 1 \times 10^6$ and $C_l = 3.40$. The multielement airfoil was designed to achieve a given C_l such that a reduction in C_d is achieved for a given C_l, and not the trivial reduction in C_d due to decreased C_l. Efforts in this design were focused upon the design of an improved main-element airfoil. The flap coordinates, chord lengths, gap sizes, and overhang distances remained unchanged relative to the baseline MFFS(ns)-026 airfoil. However, the relative flap deflection angles are defined to be slightly different when compared to the baseline airfoil. Efforts were taken to match C_l for the designed airfoil to the baseline airfoil through minor changes in α and δ_r. A geometric design constraint was imposed such that the main-element $(t/c)_{max}$ remained unchanged and defined to be 0.14 based upon the system chord length or 0.20 based upon the elemental chord length $(0.700c)$.

Careful analysis of the MFFS(ns)-026 performance suggested the design could be improved in numerous respects. Most significantly, it was desired to obtain improved aerodynamic performance by decreasing the strength of wake bursting. It is known that the size of a wake at a given $\widetilde{x}$ is a function of both the initial wake thickness (resulting from the boundary layers shed into the wake) and the magnitude of the adverse pressure gradient applied to the wake. It is thus obvious that smaller and thinner boundary layers yield a thinner wake for the same pressure gradient. In addition, a strong adverse pressure gradient yields a larger, thicker wake than that of a weaker adverse pressure gradient. Consequently, increased pressure recovery over the main element decreases the strength of the off-the-surface adverse pressure gradient applied to the wake. Thus, the size of a wake can be reduced through thinner boundary layers and weaker adverse pressure gradients.

In this section, the design parameters and elemental airfoil shapes of an improved main-element airfoil are presented. Results from the new airfoil are compared to the baseline three-element MFFS(ns)-026 airfoil. A discussion of the computationally-predicted flowfield at the design point evidences the improved aerodynamic performance of the flowfield. Finally, the improved flowfield is quantified by numerous advanced wake metrics.

A. Airfoil A4 Geometry and Transition Points

As previously mentioned, a new main-element airfoil was designed to improve aerodynamic performance at the design point by decreasing wake thickness and momentum loss relative to the baseline airfoil. The airfoil, named A4, was designed using the MFOIL/PROFOIL multipoint inverse-design routine discussed in Sec. II D. The inverse-design parameters used to design airfoil A4 are shown in Table 6 and Fig. 16(a,b) relative to the baseline MFFS(ns)-026. The airfoil geometries and MSES-predicted pressure distributions are presented for both airfoils in Fig. 16(c). As seen in Fig. 16(c), the flow around the forward portion of the upper surface is subjected to a significantly weaker adverse pressure gradient than that of the MFFS(ns)-026. Meticulous modifications of a variety of airfoil-design parameters were implemented to achieve this pressure distribution. These parameters, tabulated in Table 6, and the specified α^*-ϕ distributions were used to design the new airfoil. As shown in Table 6, a decrease in K_u for airfoil A4 results in a weaker $\partial C_p/\partial \widetilde{x}$ at the beginning of the pressure-recovery region than the baseline airfoil. In addition, reduced C_{m_0} results in a more-aft-loaded airfoil. Finally, the somewhat-large change in K_s modifies the pressure distribution near such that $\partial C_p/\partial \widetilde{x}$ for both the upper and lower surface is decreased immediately upstream of the main-element trailing edge. These three design choices, in addition to the specified α^*-ϕ distributions, resulted in a much weaker adverse pressure gradient in the forward portion of the main-element upper surface. This pressure gradient is reduced through the combination of two different effects. First, the magnitude of the pressure peak is reduced for airfoil A4 relative to the MFFS(ns)-026, thus resulting in decreased pressure that must be recovered over the main element. In addition, the point of rapid pressure recovery is moved in a downstream direction when compared to the MFFS(ns)-026. As seen in Table 7, the laminar-to-turbulent transition point is moved in a downstream direction for airfoil A4 relative to the baseline case, and this movement is partially attributed to the weaker pressure gradient. This increased laminar run results in improved aerodynamic performance and a thinner boundary layer than for a flow with a shorter laminar run. The reader is reminded that free-transition simulations in MSES were used to calculate these transition locations. In addition to the boundary-layer development over the main element, the off-the-surface pressure recovery is reduced for airfoil A4 when compared to the baseline. Pressure is dumped from the main element of airfoil A4 at C_p of -1.03 while the baseline airfoil dumps the flow at $C_p = -1.09$.

Table 6. Inverse-Design Parameters for MFFS(ns)-026 and A4

	MFFS(ns)-026 Main Element	A4 Main Element
K_u	0.05	0.02
K_l	0.20	0.20
K_s	0.30	0.50
C_{m_0}	-0.20	-0.15
$(t/c)_{max}$	0.200	0.200

B. Airfoil A4 RANS Results

Computational simulations of airfoil A4, incorporating the transition points listed in Table 7, were executed in USM3D, and the results are shown in Fig. 17. A detailed view showing part of flap 1 and the entirety of flap 2 is presented for both the MFFS(ns)-026 and A4 airfoils. Meticulous examination of these two plots indicates that the main-element wake of airfoil A4 is thinner than that of the MFFS(ns)-026 airfoil. Despite the noticeably-smaller main-element wake, the size of the flap 1 wake is observed to slightly increase in size relative to the baseline. It is noted, however, that main-element wake for both airfoils rapidly thickens at $\widetilde{x} \approx 0.95$, as discussed in detail later in this section. Despite the similar points of rapid wake growth, the A4 airfoil main-element wake grows less than that of the MFFS(ns)-026 main-element wake. Finally, the flow over the upper surface of flap 2 is fully attached, unlike that of the MFFS(ns)-

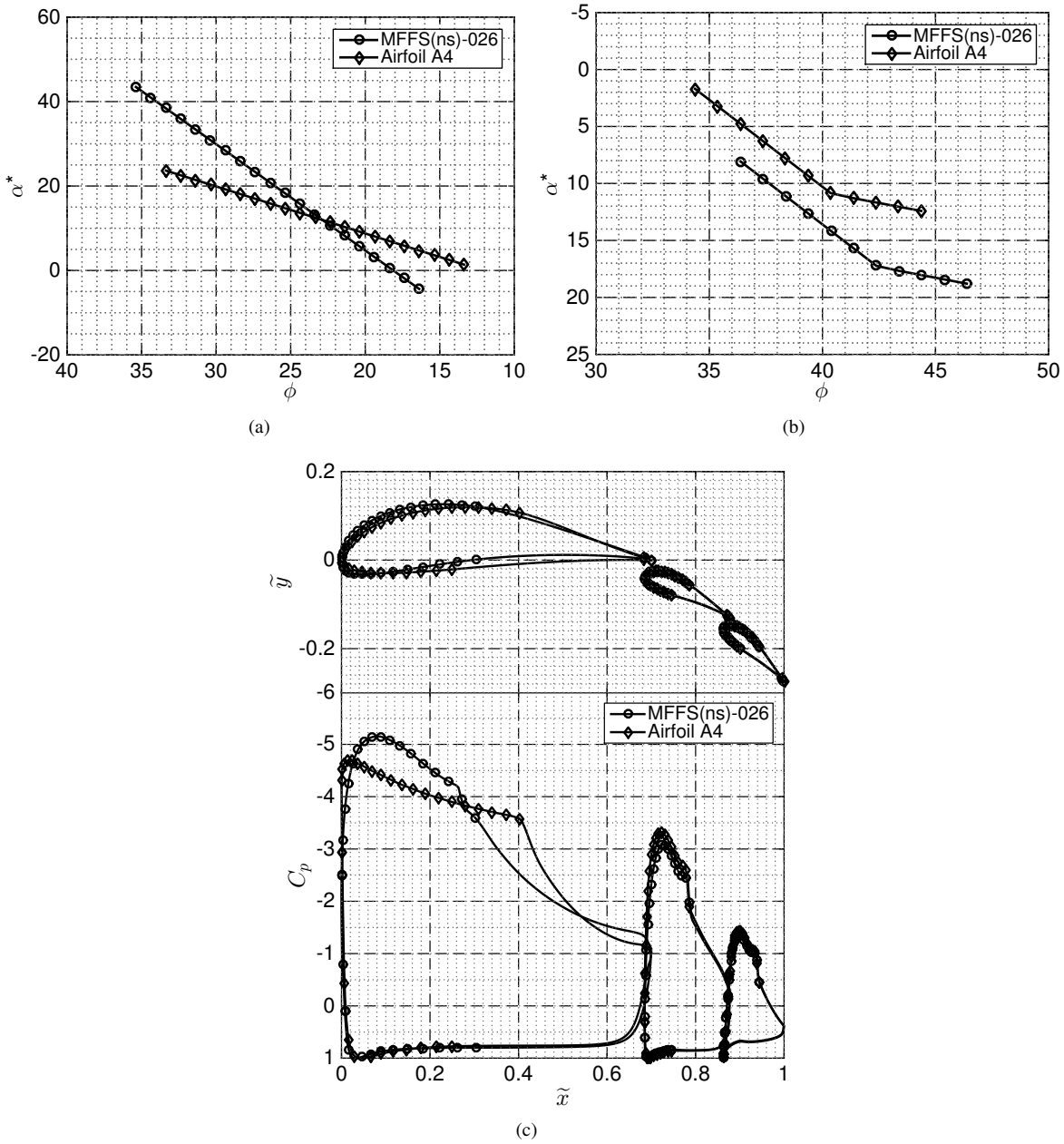

Figure 16. Specified α^*-ϕ distribution for A4 (diamonds) and MFFS(ns)-026 (circles) for (a) main-element upper surfaces, (b) main-element lower surfaces, and (c) resulting geometries and MSES-predicted pressure distributions coplotted with ϕ control points.

026 results. Improved aerodynamic performance, resulting from improved boundary-layer development and decreased wake thickness, is increased to a C_l/C_d of 77.5, or an 8.6% increase relative to the MFFS(ns)-026. Thus it can be seen that the effect upon C_d due to the increased thickness of the flap 1 wake is weaker than the effect of increased laminar-run distance, a thinner main-element wake, and attached flow over the flap 2 upper surface. Wake profiles, quantified by $\widetilde{U}_t$, for the two airfoils at $\widetilde{x}$ values of 1.10 and 1.30 are plotted in Fig. 18. In the figure, A4 data are plotted with dashed lines while solid lines represent MFFS(ns)-026 results. Small circles and triangles indicate data at $\widetilde{x}$ of 1.10 and 1.30, respectively. The figure clearly shows that both the magnitude of the momentum deficit and the width of the wake are decreased for A4 relative to that of the baseline airfoil. This result is observed at both $\widetilde{x}$ positions.

Table 7. Transition Points ($\widetilde{x}$) for MFFS(ns)-026 and A4 at $C_l = 3.40$ and $Re = 1 \times 10^6$

		MFFS(ns)-026	A4
Main Element	Upper Surface	0.263	0.400
	Lower Surface	0.700 (trailing edge)	0.700 (trailing edge)
Flap 1	Upper Surface	0.783	0.779
	Lower Surface	0.876 (trailing edge)	0.877 (trailing edge)
Flap 2	Upper Surface	0.937	0.937
	Lower Surface	1.000 (trailing edge)	1.000 (trailing edge)

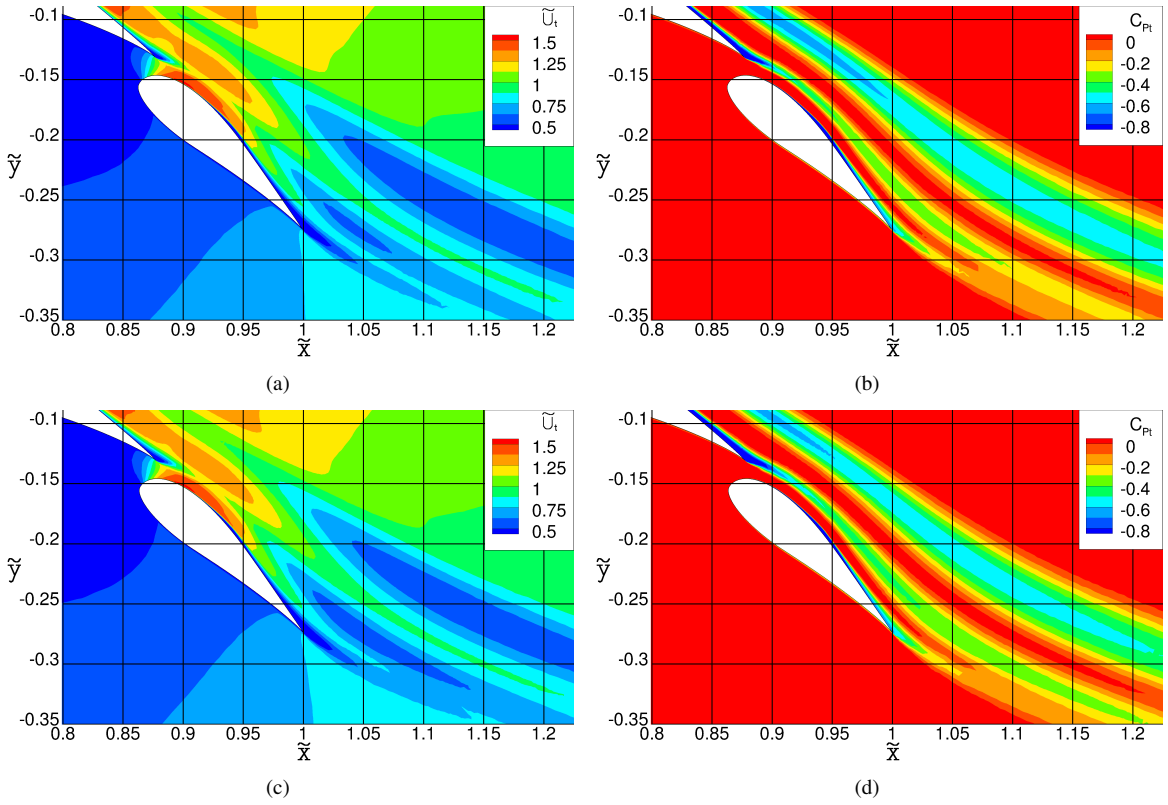

Figure 17. Computational results at $C_l = 3.40$ and $Re = 1 \times 10^6$ for flow near trailing edge of (a) MFFS(ns)-026 $\widetilde{U}_t$, (b) MFFS(ns)-026 $C_{p,t}$, (c) A4 $\widetilde{U}_t$, and (d) A4 $C_{p,t}$.

C. Airfoil A4 Wake Metrics

Advanced wake metrics, as presented in Sec. III D, were used to quantify the burst-wakes of the MFFS(ns)-026 and A4 airfoils. The burst point for airfoil A4 at α of 0 deg and Re of 1×10^6 was determined to be $\widetilde{x}_b = 0.952$, which is slightly upstream of the MFFS(ns)-026, which was calculated to be $\widetilde{x}_b = 0.954$. The strength of wake bursting for airfoil A4 was calculated to be $\widetilde{s} = 0.0056$, a 41% reduction from $\widetilde{s} = 0.0095$ for the MFFS(ns)-026. This decreased strength of wake bursting is further evidence of the improved performance of airfoil A4 relative to the baseline airfoil.

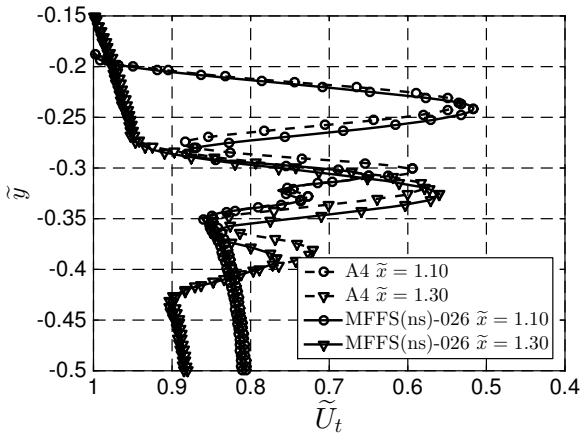

Figure 18. Wake profiles for A4 and MFFS(ns)-026 at $\widetilde{x}$ of 1.10 and 1.30.

V. Main-Element Modifications at Re $= 3 \times 10^6$

Similar to the previous airfoil design, Fig. 10 indicates severe wake bursting for the main-element wake and moderate bursting for the flap 1 wake. These features adversely affect the aerodynamic performance of the airfoil. Consequently, a second airfoil was designed in which only the main element was modified for a target C_l of 3.40 and Reynolds number of 3×10^6. No changes were made to the flap coordinates, gap size, or overhang distance. Similar to airfoil A4, the main-element $(t/c)_{max}$ was prescribed to be 0.14 based upon the system chord length (or 0.20 based upon the elemental chord length). Numerous design decisions were made such that the aerodynamic performance of the newly-designed airfoil is superior to that of the MFFS(ns)-026.

A. Airfoil B6 Geometry and Transition Points

A newly-developed main-element, designed as specified in Table 8 and Fig. 19, was substituted for the MFFS(ns)-026 main-element airfoil. As shown in Table 8, increased K_u and K_s improved the pressure distribution near the main-element trailing edge which, in part, dumps the pressure at increased C_p relative to the MFFS(ns)-026 airfoil as seen in Fig. 19(c). More specifically, the pressure is dumped from the main element of the MFFS(ns)-026 airfoil at $C_p = -1.07$ while C_p is dumped from the main element of airfoil B6 at C_p of -0.738. The increased pressure recovery over the main-element airfoil reduces the off-the-surface pressure recovery in the wake region, thus subjecting the wake to a weaker $\partial C_p/\partial \widetilde{x}$. As was the case for airfoil A4, airfoil B6 is characterized by a very broad pressure peak and a very weak adverse pressure gradient in the forward portion of the airfoil. This pressure peak was flattened through improved α^*-ϕ curves, slightly reduced C_{m_0}, and the additional specification of maximum camber. While the zero-lift pitching moment remained relatively unchanged relative to MFFS(ns)-026, the additional constraint to define the maximum camber value was used to more-readily control the C_p distribution in the forward part of the main element. As seen in the figure, the transition point for the main-element upper surface is moved downstream compared to the baseline airfoil, as presented in Table 9. Once again, laminar-to-turbulent flow transition was not observed in the lower surface of any airfoil element.

B. Airfoil B6 RANS Results

Figure 20 presents unstructured RANS computations for both the MFFS(ns)-026 and airfoil B6 at $C_l = 3.40$ and $Re = 3 \times 10^6$ as evidenced by $\widetilde{U}_t$ and $C_{p,t}$. As seen in the figure, the main-element wake is burst for both airfoils, but no significant differences are observed for the flap 1 or flap 2 wakes between the two airfoils. Results indicate that the B6 main-element wake is actually slightly larger and thicker than that of the MFFS(ns)-026. Despite this thicker wake, airfoil B6 yields an increase in C_l/C_d of 8.32% relative to the baseline airfoil. Consequently, it is observed that the boundary-layer development over the airfoils, and thus also the transition location, must be simultaneously considered with the burst-wake region. Thus, the best airfoil for a given condition may not be an airfoil that minimizes the wake thickness.

Table 8. Inverse-Design Parameters for MFFS(ns)-026 and B6

	MFFS(ns)-026 Main Element	B6 Main Element
K_u	0.05	0.20
K_l	0.20	0.20
K_s	0.30	0.50
C_{m_0}	−0.20	−0.21
$(t/c)_{max}$	0.200	0.200
$camber_{max}$	–	0.11

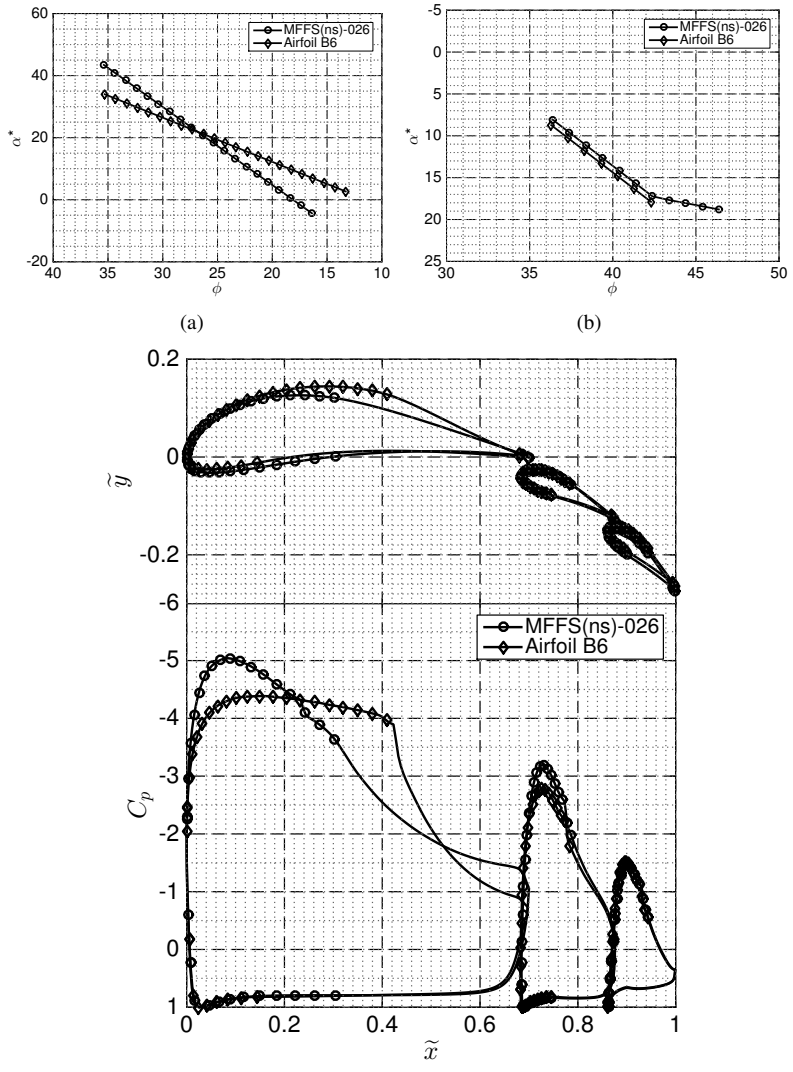

Figure 19. Specified α^*-ϕ distribution for MFFS(ns)-026 (red triangles) and B6 (lavender circles) including (a) main-element upper surface, (b) main-element lower surface, and (c) resulting geometry and C_p curves coplotted with control points.

Table 9. Transition Points ($\widetilde{x}$) for MFFS(ns)-026 and B6 at $\alpha = 0$ deg and $Re = 3 \times 10^6$

		MFFS(ns)-026	B6
Main Element	Upper Surface	0.222	0.419
	Lower Surface	0.700 (trailing edge)	0.700 (trailing edge)
Flap 1	Upper Surface	0.773	0.776
	Lower Surface	0.876 (trailing edge)	0.874 (trailing edge)
Flap 2	Upper Surface	0.931	0.929
	Lower Surface	1.000 (trailing edge)	1.000 (trailing edge)

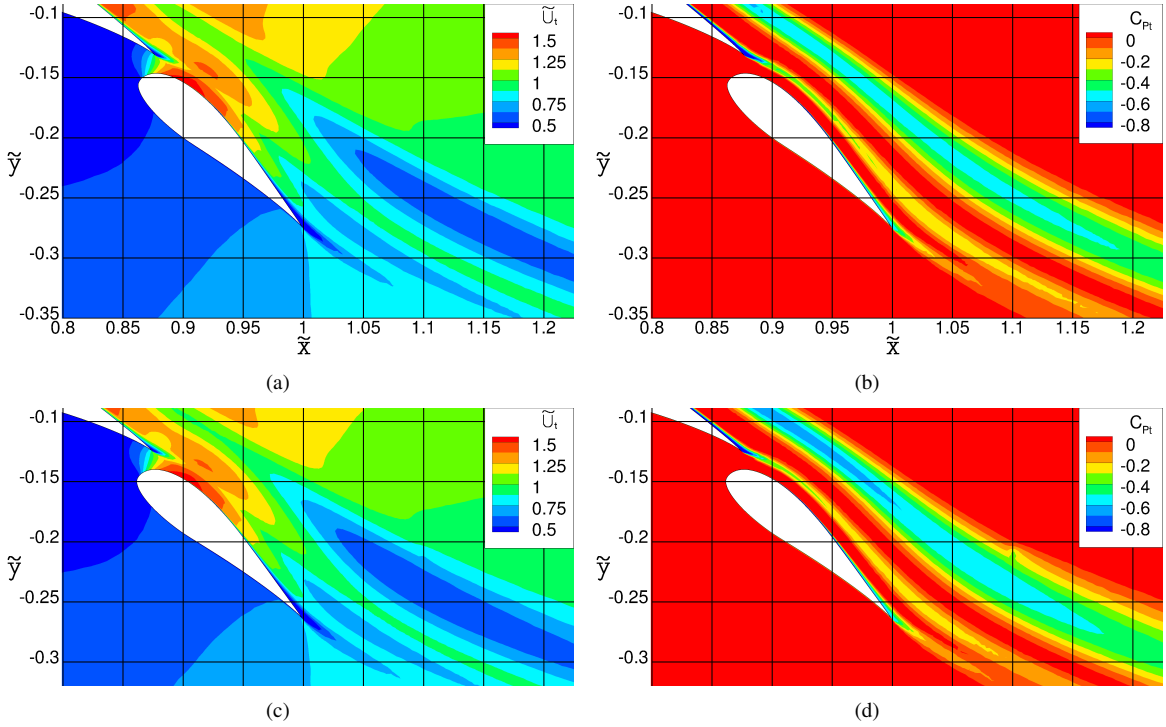

Figure 20. Computational results at $C_l = 3.40$ and $Re = 3 \times 10^6$ for flow near trailing edge of (a) MFFS(ns)-026 $\widetilde{U}_t$, (b) MFFS(ns)-026 $C_{p,t}$, (c) B6 $\widetilde{U}_t$, and (d) B6 $C_{p,t}$.

C. Airfoil B6 Wake Metrics

Similar to airfoil A4, wake metrics were calculated to quantify burst-wake parameters including both the burst point and strength of wake bursting. Results indicate that both airfoil B6 and MFFS(ns)-026 burst at $\widetilde{x}_b = 0.952$ for $C_l = 3.40$ and $Re = 3 \times 10^6$. The reader is reminded that very little change in $\widetilde{x}_b$ was observed between airfoil A4 and the baseline airfoil for Re of 1×10^6. As was previously observed in Fig. 20, the main-element wake of airfoil B6 is thicker than that of the MFFS(ns)-026 airfoil. Thus, even though airfoil B6 yields superior C_l/C_d relative to the MFFS(ns)-026, airfoil B6 yields increased wake bursting. More specifically, $\widetilde{s}$ is observed to increase from 0.0056 to 0.0073 for the baseline and B6 airfoils, respectively.

VI. All Airfoil Element Modifications at Re $= 1 \times 10^6$

Building upon knowledge gained through the design of airfoil A4, a design exercise was completed in which neither the coordinates and nor position of either flap was constrained. This three-element airfoil, designed for $Re = 1 \times 10^6$

and $C_l = 3.40$, included $(t/c)_{max}$ of 0.14 and relative chord lengths were defined to be 0.700, 0.213, and 0.182 for the main element, flap 1, and flap 2, respectively. These chord lengths remain unchanged relative to the baseline MFFS(ns)-026 airfoil tabulated in Table 2.

A. Airfoil C5

A final airfoil, denoted as the C5 airfoil, was designed for a target Reynolds number of 1×10^6 and C_l of 3.40. Contrary to the two previous airfoil designs, the flap coordinates and positions were not constrained to be the same as the MFFS(ns)-026 airfoil. While the flap chord ratios were defined to be the same as the baseline airfoil, all other design constraints were relaxed. Design constraints were specified such that $(t/c)_{max}$ for the main element was constrained to be 0.20 based upon the elemental chord length.

B. Airfoil C5 Geometry and Transition Points

The C5 three-element airfoil was designed with the α^*-ϕ curves plotted in Fig. 21 and design parameters listed in Table 10. While the aforementioned airfoil A4, comprised of a redesigned main element for a target Reynolds number of 1×10^6 and C_l of 3.40, yielded improved aerodynamic performance relative to the baseline airfoil, further efforts improved the aerodynamic performance by redesigning all three airfoil elements. As listed in Table 10, significant changes were made to the K_u and K_l recovery factors in addition to changes in the zero-lift pitching moment for airfoil C5 when compared to airfoil A4. Decreased K parameters for both the upper and lower surfaces relative to the baseline airfoil result in increased pressure recovery over the main element. Because of the increased main-element pressure recovery, a weaker adverse pressure gradient was applied to the wake. While previous knowledge indicates the pressure may be recovered more efficiently in the wake region than over the airfoil surface, it is observed that a stronger streamwise pressure gradient in the wake may lead to wake bursting if too much pressure is recovered in the viscous wake. As seen in Fig. 21(g), airfoil C5 was designed with a very weak pressure peak and a weak adverse pressure gradient for the forward portion of the main element upper-surface flow. The α^*-ϕ curves shown in Fig. 21 present both the MFFS(ns)-026 and C5 airfoils. A shallower α^*-ϕ curve over the main-element upper surface decreased the adverse pressure gradient for $\widetilde{x} \leq 0.48$ thus leading to an increased laminar run and thinner boundary layer at the transition point. In addition, the decreased K also resulted in increased C_p at the main-element trailing edge and therefore decreased the pressure recovery in the wake. The two thinner flaps were slightly unloaded relative to the baseline case, as evidenced in the C_p distributions. The laminar-to-turbulent transition points, visible in Fig. 21(g), are detailed in Table 11 for both the MFFS(ns)-026 and C5 airfoils. As seen in the table, airfoil C5 exhibits superior laminar flow relative to the baseline case thus resulting in a improved aerodynamic performance.

Table 10. Inverse-Design Parameters for MFFS(ns)-026 and C5 Airfoils

	MFFS(ns)-026			Airfoil C5		
	Main Element	Flap 1	Flap 2	Main Element	Flap 1	Flap 2
K_u	0.05	0.20	0.20	0.02	0.02	0.20
K_l	0.20	0.20	0.20	0.02	0.02	0.20
K_s	0.30	0.15	0.14	0.50	0.50	0.40
C_{m_0}	−0.20	−0.16	−0.10	−0.175	−0.21	−0.14
$(t/c)_{max}$	0.200	0.205	0.205	0.200	–	–
gap	–	0.0259	0.0152	–	0.026	0.018
$overhang$	–	0.0154	0.002	–	0.015	0.007
δ_r	–	26.3	16.3	–	26.1	16.1

C. Airfoil C5 RANS Results

Computational results for the baseline MFFS(ns)-026 airfoil and redesigned airfoil C5 are shown in Fig. 22 at the design point of $C_l = 3.40$ and $Re = 1 \times 10^6$. Results, including both $\widetilde{U}_t$ and $C_{p,t}$, indicate the main-element and flap 1 wakes shed from C5 are markedly smaller and thinner than that of the baseline MFFS(ns)-026. In addition to the

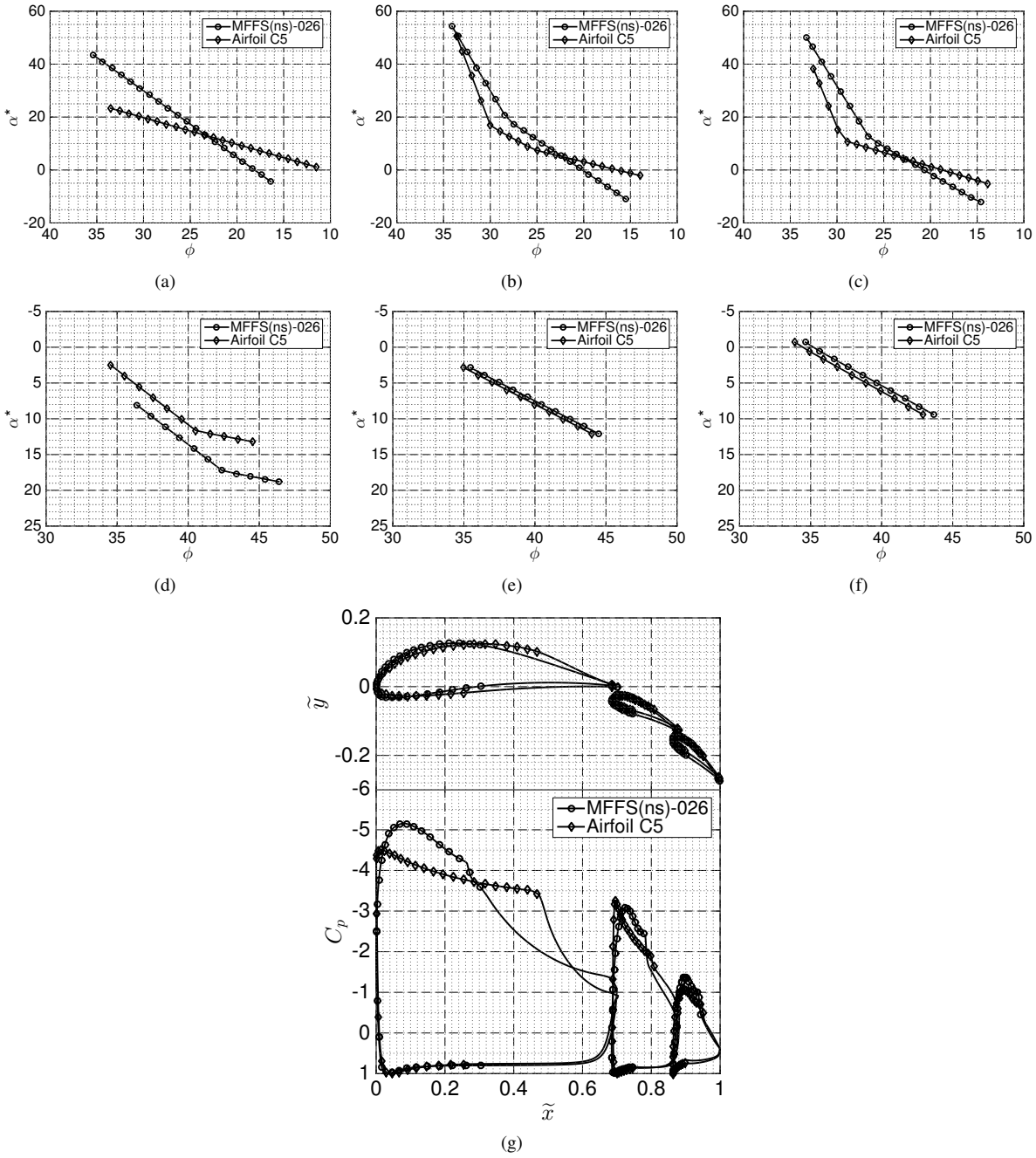

Figure 21. Specified α^*-ϕ distribution for MFFS(ns)-026 (triangles) and C5 (circles) airfoils including (a) main-element upper surface, (b) flap 1 upper surface, (c) flap 2 upper surface, (d) main-element lower surface, (e) flap 1 lower surface, (f) flap 2 lower surface, and (g) resulting geometry coplotted with control points.

thinner wake, the difference in $\widetilde{U}_{t_{min}}|_{\widetilde{x}}$, calculated to be and 0.509 and 0.554 for the baseline and C5 airfoils, indicates less momentum is lost for C5 than for the baseline airfoil. The improved flowfield results in C_l/C_d at the design point to be 84.5, which is 16.9% higher than the baseline and 8.52% higher than the A4 airfoils.

D. Airfoil C5 Wake Metrics

Advanced wake metrics, including the burst point and the magnitude of wake bursting as defined in Sec. III D, for airfoil C5 were determined. As is the case for the previously-discussed A4 and B6 results, the burst point for airfoil

Table 11. Transition Points ($\widetilde{x}$) for MFFS(ns)-026 and C5 at $\alpha = 0$ deg and $Re = 1 \times 10^6$

		MFFS(ns)-026	C5
Main Element	Upper Surface	0.263	0.475
	Lower Surface	0.700 (trailing edge)	0.700 (trailing edge)
Flap 1	Upper Surface	0.783	0.798
	Lower Surface	0.876 (trailing edge)	0.881 (trailing edge)
Flap 2	Upper Surface	0.937	0.947
	Lower Surface	1.000 (trailing edge)	1.000 (trailing edge)

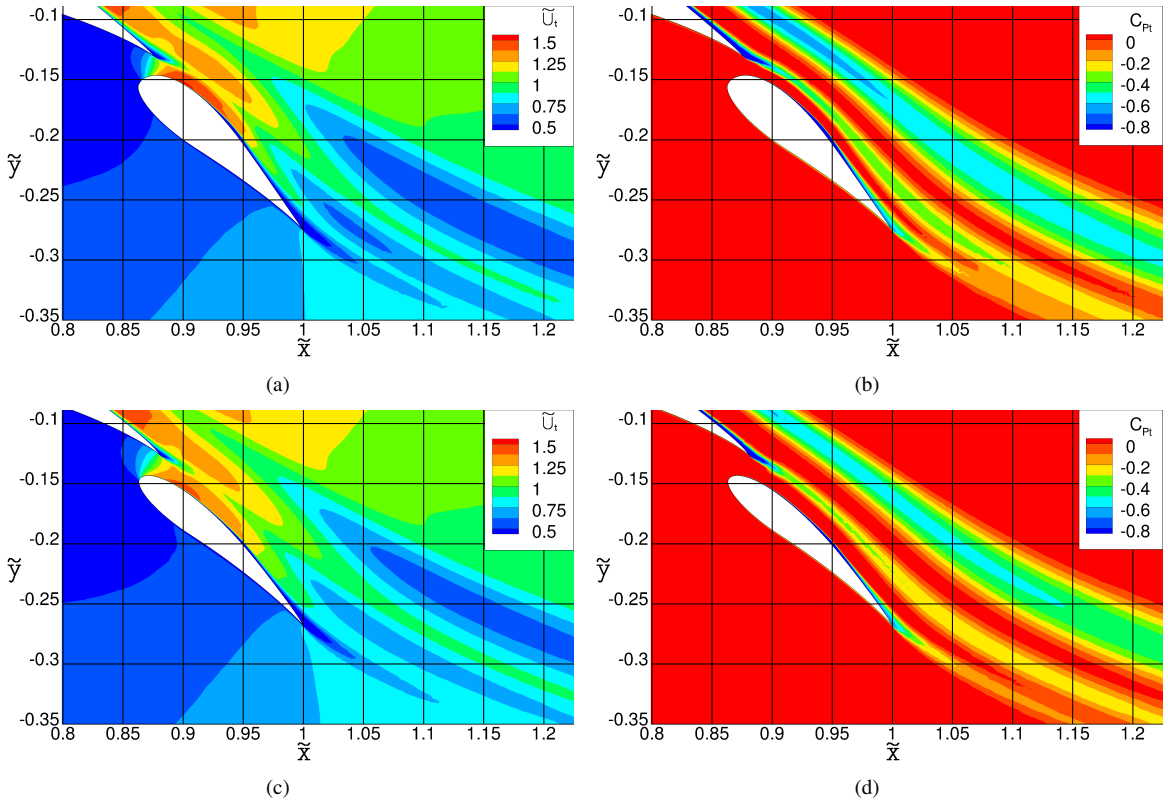

Figure 22. Computational results at $C_l = 3.40$ and $Re = 1 \times 10^6$ for flow near trailing edge of (a) MFFS(ns)-026 $\widetilde{U}_t$, (b) MFFS(ns)-026 $C_{p,t}$, (c) C5 $\widetilde{U}_t$, and (d) C5 $C_{p,t}$.

C5, calculated to be $\widetilde{x}_b = 0.953$, is only slightly upstream of the MFFS(ns)-026 burst point of $\widetilde{x}_b = 0.954$. The location of this burst point can also be qualitatively observed in Fig. 22 through examination of the $\widetilde{U}_t$ contours. The main-element wake is stated to be moderately burst as $\widetilde{s}$ was determined to be 0.0050, a 47% reduction from the baseline results.

VII. Conclusions

Three multielement airfoils were designed using inverse-design conformal-mapping techniques to reduce the presence of wake bursting and improve aerodynamic performance when compared to a baseline three-element airfoil. Computational simulations, using an inviscid/viscous coupled routine and also an unstructured RANS code, were executed for the designed airfoils to quantify the performance benefit of each airfoil. Two of these three multielement

airfoils, comprised of a redesigned main-element airfoil, were developed for a design point of C_l of 3.40 and Re of 1×10^6 and 3×10^6, respectively. An increase in C_l/C_d at the design point was found to be approximately 8% for each of these two airfoils. A third airfoil, for a target Re of 1×10^6, was designed incorporating new coordinates for all three elements and new flap rigging locations. This airfoil yielded a net increase in C_l/C_d of nearly 17% from the baseline airfoil.

Two novel wake metrics are proposed to quantify burst-wake behavior. One parameter, defined from the behavior of total-pressure isolines, defines the point at which a wake is said to be burst. The second metric, also defined from total-pressure contour lines, defines the extent of wake bursting. That is, this metric defines whether a wake is slightly, moderately, or severely burst. Results indicate that improved performance of a newly-designed airfoil is increased through the simultaneous consideration of both the transition point and the wake behavior. While smaller and thinner wakes are typically indicative of less momentum loss, improved laminar boundary-layer behavior over the main-element could offset a slight increase in wake thickness. In addition, it is observed that wake width is not necessarily a sufficiently-robust metric to quantify wake bursting, but also the minimum velocity within the wake must also be considered.

Acknowledgments

Support for this research project was provided by National Science Foundation graduate research fellowship grant number 07-15088 and through a University of Illinois Graduate College Dissertation Completion Fellowship.

References

[1]Mack, M. D. and McMasters, J. H., "High Reynolds Number Testing in Support of Transport Airplane Development," AIAA Paper 92-3982, AIAA Aerospace Ground Testing Conference, Nashville, TN, 1992.

[2]Nakayama, A., Kreplin, H. P., and Morgan, H. L., "Experimental Investigation of Flowfield About a Multielement Airfoil," *AIAA Journal*, Vol. 28, No. 1, 1988, pp. 14–21.

[3]Driver, D. M. and Mateer, G. G., "Wake Flow in Adverse Pressure Gradient," *International Journal of Heat and Fluid Flow*, Vol. 23, 2002, pp. 564–571.

[4]Hoffenberg, R. and Sullivan, J. P., "Measurement and Simulation of Wake Deceleration," AIAA Paper 98-0522, AIAA Aerospace Sciences Meeting, Reno, NV, 1998.

[5]Pomeroy, B. W., Ansell, P. J., Diebold, J. M., and Selig, M. S., "A Study of Burst Wakes in a Multielement Airfoil Flowfield," AIAA Paper 2013-2919, AIAA Applied Aerodynamics Conference, San Diego, CA, 2013.

[6]Pomeroy, B. W., Diebold, J. M., Ansell, P. J., and Selig, M. S., "Study of Burst Wakes in a Multielement Airfoil Flowfield," *AIAA Journal*, Vol. 52, No. 4, April 2014, pp. 821–831.

[7]Smith, A. M. O., "High-Lift Aerodynamics," *Journal of Aircraft*, Vol. 12, No. 6, 1975, pp. 501–530.

[8]Klausmeyer, S. M. and Lin, J. C., "An Experimental Investigation of Skin Friction on a Multi-Element Airfoil," AIAA Paper 94-1870, AIAA Applied Aerodynamics Conference, Colorado Springs, CO, 1994.

[9]Hoffenberg, R. and Sullivan, J. P., "Simulation of High-Lift Wake Behavior," AIAA Paper 97-0718, AIAA Aerospace Sciences Meeting, Reno, NV, 1997.

[10]Pomeroy, B. W., Williamson, G. A., and Selig, M. S., "Experimental Study of a Multielement Airfoil for Large Wind Turbines," AIAA Paper 2012-2892, AIAA Applied Aerodynamics Conference, New Orleans, LA, 2012.

[11]Valarezo, W. O., Dominik, C. J., and McGhee, R. J., "Multielement Airfoil Performance Due to Reynolds and Mach Number Variations," *Journal of Aircraft*, Vol. 30, No. 5, 1993, pp. 689–694.

[12]Pomeroy, B. W. and Selig, M. S., "Pressure Measurements of Burst Wakes Over a Three-Element Airfoil," AIAA Paper 2015-2569, AIAA Applied Aerodynamics Conference, Dallas, TX, 2015.

[13]Spaid, F. W., "High Reynolds Number, Multielement Airfoil Flowfield Measurements," *Journal of Aircraft*, Vol. 37, No. 3, 2000, pp. 499–507.

[14]Rogers, S. E., "Progress in High-Lift Aerodynamic Calculations," *Journal of Aircraft*, Vol. 31, No. 6, 1994, pp. 1244–1251.

[15]Cebeci, T., Besnard, E., and Chen, H. H., "Calculation of Multielement Airfoil Flows, Including Flap Wells," AIAA Paper 96-0056, AIAA Aerospace Sciences Meeting, Reno, NV, 1996.

[16]Czerwiec, R. and Edwards, J. R., "Theory and Experiment of Multielement Airfoils – A Comparison," AIAA Paper 2000-0985, AIAA Aerospace Sciences Meeting, Reno, NV, 2000.

[17]Narsipur, S., Pomeroy, B. W., and Selig, M. S., "CFD Analysis of Multielement Airfoils for Wind Turbines," AIAA Paper 2012-2781, AIAA Applied Aerodynamics Conference, New Orleans, LA, 2012.

[18]Wang, G., Liu, Y., Mian, H. H., and Ye, Z.-Y., "A NUFFT Technique for Flow Fluctuation Analysis Based on the Unsteady Flow Simulation with Variable Physical Time Stepping Scheme," AIAA Paper 2014-3251, AIAA Applied Aerodynamics Conference, Atlanta, GA, 2014.

[19]Chin, V. D., "Flowfield Measurements about a Multi-Element Airfoil at High Reynolds Numbers," AIAA Paper 93-3137, AIAA Fluid Dynamics Conference, Orlando, FL, 1993.

[20]Pomeroy, B. W., *Wake Bursting: A Computational and Experimental Investigation for Application to High-Lift Multielement Airfoil Design*, Ph.D. thesis, University of Illinois at Urbana-Champaign, Department of Aerospace Engineering, 2016.

[21]Schneider, S., Campbell, B., Bucci, G., and Sullivan, J. P., "An Experimental Simulation of Flap Flow on Multielement Airfoils at High Reynolds Number," AIAA Paper 94-2613, AIAA Aerospace Ground Testing Conference, Colorado Springs, CO, 1994.

[22]Hoffenberg, R., Sullivan, J. P., and Schneider, S., "Wake Measurements in a Strong Adverse Pressure Gradient," NASA CR 197272, 1995.

[23]Bucci, G. S. and Sullivan, J. P., "An Experimental Simulation of High Lift Wake Flows at High Reynolds Number," AIAA Paper 97-2297, AIAA Applied Aerodynamics Conference, Atlanta, GA, 1997.

[24]Slotnick, J. P., Hannon, J. A., and Chaffin, M., "Overview of the First AIAA CFD High Lift Prediction Workshop," AIAA Paper 2011-862, AIAA Aerospace Sciences Meeting, Orlando, FL, 2011.

[25]Rumsey, C. L., Slotnick, J. P., Long, M., Stuever, R. A., and Wayman, T. R., "Summary of the First AIAA CFD High-Lift Prediction Workshop," *Journal of Aircraft*, Vol. 48, No. 6, November 2011, pp. 2068–2079.

[26]Rumsey, C. L. and Slotnick, J. P., "Overview and Summary of the Second AIAA High Lift Prediction Workshop," AIAA Paper 2014-0747, AIAA Aerospace Sciences Meeting, National Harbor, MD, 2014.

[27]Ragheb, A. M. and Selig, M. S., "Multi-Element Airfoil Configurations for Wind Turbines," AIAA Paper 2011-3971, AIAA Applied Aerodynamics Conference, Honolulu, HI, 2011.

[28]Drela, M., *A User's Guide to MSES 3.05*, MIT Department of Aeronautics and Astronautics, July, 2007.

[29]Drela, M., *Two-Dimensional Transonic Aerodynamic Design and Analysis using the Euler Equations*, Ph.D. thesis, Massachusetts Institute of Technology, M.I.T. Report No. 187, 1986.

[30]Drela, M. and Giles, M. B., "ISES: A Two-Dimensional Viscous Aerodynamic Design and Analysis Code," AIAA Paper 86-0424, AIAA Aerospace Sciences Meeting, Reno, NV, 1986.

[31]Drela, M., Giles, M. B., and Thomkins, W. T., *Newton Solution of Coupled Euler and Boundary-Layer Equations*, Springer-Verlag, Numerical and Physical Aspects fo Aerodynamic Flows III, 1986.

[32]Giles, M. B. and Drela, M., "Two-Dimensional Transonic Aerodynamic Design Method," *AIAA Journal*, Vol. 25, No. 9, 1987, pp. 1199–1206.

[33]Mueller, T. J., editor, *XFOIL: An Analysis and Design System for Low Reynolds Number Airfoils*, Vol. 54, Springer, Low Reynolds Number Aerodynamics, Lecture Notes in Engineering, 1989.

[34]Drela, M., "Newton Solution of Coupled Viscous/Inviscid Multielement Airfoil Flows," AIAA Paper 90-1470, AIAA Fluid Dynamics, Plasma Dynamics, and Lasers Conference, Seattle, WA, 1990.

[35]Drela, M., "Improvements in Low Reynolds Number Airfoil Flow Predictions with ISES and XFOIL," Tech. rep., Massachusetts Institute of Technology, 1990.

[36]Drela, M., "Viscous and Inviscid Inverse Schemes Using Newton's Method," AGARD-FDP-VKI Lecture Series, Brussels, Belgium, 1990.

[37]Drela, M., "Design and Optimization Method for Multi-Element Airfoils," AIAA Paper 93-0969, AIAA Aerospace Design Conference, Irvine, CA, 1993.

[38]Mughal, B. and Drela, M., "A Calculation Method for the Three-Dimensional Boundary-Layer Equations in Integral Form," AIAA Paper 93-0786, AIAA Aerospace Sciences Meeting, Reno, NV, 1993.

[39]Terry, E. L., *Extension of the Aerodynamic Design Program MSES for the Simulation of Boundary Layer Suction*, Master's thesis, Delft University of Technology, 2004.

[40]Frink, N. T., Pirzadeh, S. Z., Parikh, P. C., Pandya, M. J., and Bhat, M. K., "The NASA Tetrahedral Unstructured Software System (TetrUSS)," *The Aeronautical Journal*, Vol. 104, No. 1040, October 2000, pp. 491–499.

[41]Samareh, J., "GridTool: A Surface Modeling and Grid Generation Tool," Proceedings of the Workshop on Surface Modeling, Grid Generation, and Related Issues in CFD Solutions, NASA CP-3291, May 9-11, 1995.

[42]Samareh, J., "Unstructured Grids on NURBS Surfaces," AIAA Paper 1993-3454, 1993.

[43]Pirzadeh, S. Z., "Unstructured Viscous Grid Generation by Advancing-Layers Method," *AIAA Journal*, Vol. 32, No. 8, August 1994, pp. 1735–1737.

[44]Pirzadeh, S. Z., "Three-Dimensional Unstructured Viscous Grids by the Advancing-Layers Method," *AIAA Journal*, Vol. 34, No. 1, January 1996, pp. 43–49.

[45]Pirzadeh, S. Z., "An Adaptive Unstructured Grid Method by Grid Subdivision, Local Remeshing, and Grid Movement," AIAA 1999-3255, 1999.

[46]Frink, N. T., *Three-Dimensional Upwind Scheme for Solving the Euler Equations on Unstructured Tetrahedral Grids*, Ph.D. thesis, Virginia Polytechnic and State University, 1991.

[47]Wang, Q., Massey, S. J., and Abdol-Hamid, K. S., "Implementation of Advanced Two Equation Turbulence Models in the USM3D Unstructured Flow Solver," NASA CR-2000-210102, April 2000.

[48]Selig, M. S. and Maughmer, M. D., "A Multipoint Inverse Airfoil Design Based on Conformal Mapping," *AIAA Journal*, Vol. 30, No. 5, May 1992, pp. 1162–1170.

[49]Selig, M. S. and Maughmer, M. D., "Generalized Multipoint Inverse Airfoil Design," *AIAA Journal*, Vol. 30, No. 11, November 1992, pp. 2618–2625.

[50]Gopalarathnam, A. and Selig, M. S., "A Multipoint Inverse Method for Multi-Element Airfoil Design," AIAA Paper 96-2396, 1996.

[51]Gopalarathnam, A. and Selig, M. S., "A Multipoint Viscous Design Method for Multi-Element Airfoils," AIAA Paper 98-2404, AIAA Applied Aerodynamics Conference, Albuquerque, NM, 1998.

[52]Gopalarathnam, A., *Hybrid Methods for Inverse Aerodynamic Design*, Ph.D. thesis, University of Illinois at Urbana-Champaign, 1999.

[53]Gopalarathnam, A., "Multipoint Inverse Method for Multielement Airfoil Design," *Journal of Aircraft*, Vol. 35, No. 3, May-June 1998, pp. 398–404.

[54]Saeed, F. and Selig, M. S., "A Multipoint Inverse Airfoil Design Method for Slot-Suction Airfoils," AIAA Paper 95-1857-CP, AIAA Applied Aerodynamics Conference, San Diego, CA, 1995.

[55]Broughton, B. A., *A Hybrid Inverse Design Method for Coupled Aerodynamic and Hydrodynamic Geometries*, Ph.D. thesis, University of Illinois at Urbana-Champaign, 2004.

[56]Gopalarathnam, A., Broughton, B. A., McGranahan, B. D., and Selig, M. S., "Design of Low Reynolds Number Airfoils with Trips," *Journal of Aircraft*, Vol. 40, No. 4, July-August 2003, pp. 768–775.